



King's Research Portal

Document Version
Peer reviewed version

[Link to publication record in King's Research Portal](#)

Citation for published version (APA):

Alastruey, J., Parker, K. H., & Sherwin, S. J. (2012). Arterial pulse wave haemodynamics. In S. Anderson (Ed.), *11th International Conference on Pressure Surges* (pp. 401-443). Virtual PiE Led t/a BHR Group.

Citing this paper

Please note that where the full-text provided on King's Research Portal is the Author Accepted Manuscript or Post-Print version this may differ from the final Published version. If citing, it is advised that you check and use the publisher's definitive version for pagination, volume/issue, and date of publication details. And where the final published version is provided on the Research Portal, if citing you are again advised to check the publisher's website for any subsequent corrections.

General rights

Copyright and moral rights for the publications made accessible in the Research Portal are retained by the authors and/or other copyright owners and it is a condition of accessing publications that users recognize and abide by the legal requirements associated with these rights.

- Users may download and print one copy of any publication from the Research Portal for the purpose of private study or research.
- You may not further distribute the material or use it for any profit-making activity or commercial gain
- You may freely distribute the URL identifying the publication in the Research Portal

Take down policy

If you believe that this document breaches copyright please contact librarypure@kcl.ac.uk providing details, and we will remove access to the work immediately and investigate your claim.

Arterial pulse wave haemodynamics

Jordi Alastruey¹, Kim H. Parker², Spencer J. Sherwin³

¹Department of Biomedical Engineering, Division of Imaging Sciences and Biomedical Engineering, King's College London, King's Health Partners, St. Thomas' Hospital, London SE1 7EH, UK

²Department of Bioengineering, Imperial College, London SW7 2AZ, UK

³Department of Aeronautics, Imperial College, London SW7 2AZ, UK

Abstract

The shape of the arterial pulse wave is intimately related to the physical properties of the cardiovascular system. Understanding the mechanisms underlying this relation is clinically relevant, since pulse waveforms carry valuable information for the diagnosis and treatment of disease. We overview some numerical, theoretical and experimental efforts (using *in vivo* and *in vitro* data) made in this field of research, focusing on the physical aspects of arterial pulse wave propagation in the systemic circulation. The mathematical and numerical tools that we describe are based on the one-dimensional formulation in the time-domain.

Keywords: *haemodynamics; pulse wave propagation; one-dimensional modelling; time-domain analysis; systemic circulation.*

1 Introduction

The human cardiovascular (or circulatory) system has evolved into a complex and subtle system. Its primary function is the transport of oxygen, nutrients and metabolites to all parts of the body while simultaneously removing carbon dioxide and waste products. It serves several other roles in the maintenance of body temperature, as a conduit for signalling by hormones and is crucial in the defence of the body by the immune system.

Physically the cardiovascular system consists of two synchronised pumps in parallel (the right and left heart) that pump blood, a complex fluid made up of plasma and highly deformable blood cells, through a continuous network of flexible vessels (the arteries, *microcirculation* and veins). The right heart pumps de-oxygenated blood through the *pulmonary* circulation to the lungs where it is oxygenated, returning it to the left heart. The left heart pumps the oxygenated blood through the *systemic* circulation to the rest of the body where the oxygen is used, returning it to the right heart.

The arteries are fairly thick-walled, elastic vessels that carry blood from the heart. They branch in a predominantly tree-like structure, called the *arterial tree*, although there are a number of loops (*anastomosis*) providing for some redundancy of perfusion. Arterial diameters range from 2–4 cm for the aorta and main pulmonary artery¹ down to 0.1 mm for the small arteries that perfuse the microcirculation. The microcirculation consists of *arterioles* which branch into the *capillaries* which form a complex network with vessel diameters 6–8 μm . The capillaries merge into *venules* that also merge to form the small veins. The venous system is composed of thin-walled vessels that are roughly parallel to the arterial network with merging rather than diverging branches, although there are many more loops in the venous system. For a more detailed introduction to cardiovascular anatomy and physiology we refer to [1, 2].

Cardiovascular diseases are responsible for nearly half of all deaths worldwide. The major killer is *atherosclerosis* which forms fat deposits inside blood vessels that hinder, or even stop, the flow of blood causing heart attacks and strokes (see [3, 4] for UK and EU statistics). These and other cardiovascular diseases also account for much morbidity. It is believed that mechanical stresses

¹The aorta connects the left ventricle of the heart to the systemic circulation and the pulmonary artery connects the right ventricle to the pulmonary circulation.

caused by blood flow are involved in the initiation, localisation and progression of disease. For instance, *hypertension* (high blood pressure) increases the risk of stroke, heart attack, heart failure, arterial aneurysm and chronic renal failure [5] and regions of low or oscillatory wall shear stress (WSS) are believed to be closely associated with the distribution of early *atherosclerotic lesions* [6, 7].

Arterial blood pressure and flow (or velocity) waves are generated by cardiac contraction and its interaction with the distensible arterial walls. Arteries distend to accommodate the sudden increase in blood volume caused by cardiac contraction, since blood can be approximated as an incompressible fluid in arteries. When the elastic energy generated during distension is released, arteries contract. Therefore, arteries present a regular beating, called the *pulse*, that follows the heartbeat and propagates in the form of waves, called *pulse waves*. These produce continuous changes in blood pressure and velocity, which can be studied as pressure and velocity waves running forth and back (away from and towards the heart, respectively), with backward waves originating from the reflection² of forward waves at branching sites, peripheral impedances, and any other sites of variation in arterial geometry and elastic properties.

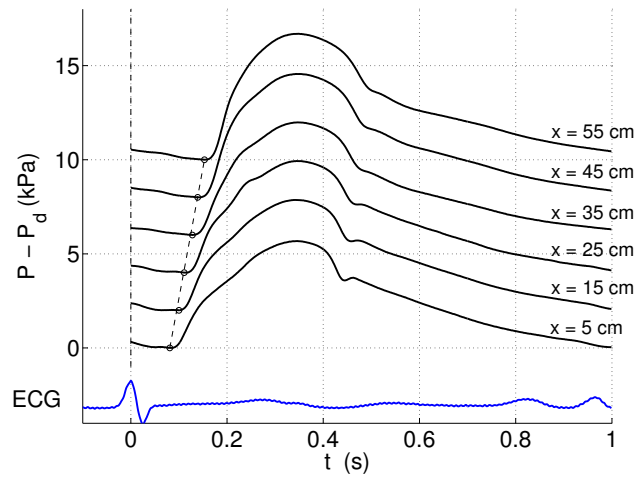


Figure 1: Blood pressure, P , waveform measured along the human aorta. Each waveform is an ensemble average of continuous pressure measurements over 1 min using the peak of the R-wave of the *electrocardiogram* (ECG) (shown at the bottom of the figure) as the reference time. Measurements were made every 10 cm down the aorta starting approximately 5 cm from the aortic valve. The circles indicate the time of the minimum pressure (the *diastolic* pressure, P_d) after which the pressure increases because of the contraction of the left ventricle. The slope of the dotted line connecting the circles indicates the pulse wave speed with which the pressure wave is propagating down the aorta.

Figure 1 shows the typical pressure waveforms measured along the human aorta in normal conditions, going from the aortic root down to the end of the aorta, where it bifurcates into the two iliac arteries that perfuse the legs (Segments 42 and 43 in Fig. 2, centre). The slope of the feet of these waves clearly shows that blood pressure at the start of *systole* (the phase of the cardiac cycle when the heart muscle is contracting) is propagating away from the heart. The propagation speed of pulse waves relative to the blood at rest is called the *pulse wave speed*, which is about 5 m s^{-1} at the ascending aorta, increases toward peripheral arteries, and is at least one order of magnitude higher than blood velocity in normal conditions³.

Pressure and flow waveforms depend on the physical properties of the cardiovascular system, such as the arterial geometry and distensibility, the flow ejected by the heart, and the impedance due to the smallest blood vessels (the *microcirculation*). Knowledge of these properties can be valuable for the diagnosis and treatment of disease. For example, the pulse wave speed is a

²This is similar to the reflection of sound waves from a surface back to the listener, which form an echo.

³Thus, during a typical heartbeat at rest, which takes about 1 s, a pulse wave has sufficient time to travel from the heart to the peripheral branches in Fig. 2 (centre) and get reflected back to the heart more than ten times.

measure of arterial stiffness, which has been identified as an important predictor of cardiovascular events that cause morbidity and mortality [8, 9].

It seems clear, therefore, that understanding the *haemodynamics* (or perhaps more accurately the pulse wave dynamics) underlying how the shapes of pressure and flow waves relate to the physical properties of the cardiovascular system is clinically relevant. This understanding can be achieved through *in vivo* experiments in humans and animals and using *in vitro*, theoretical and numerical models, ideally tested against *in vivo* data. Models allow us to answer haemodynamic questions that cannot be addressed *in vivo*, due to ethical, technical and physiological reasons⁴, and disentangle their underlying mechanisms.

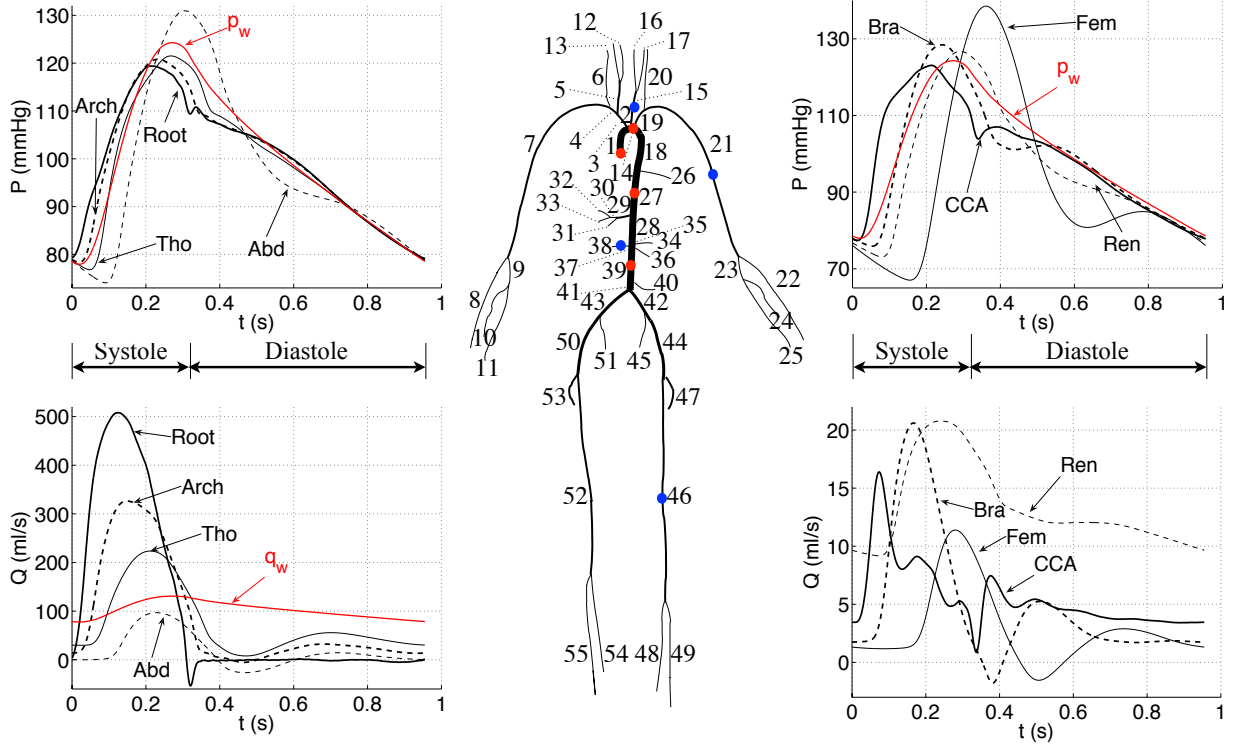


Figure 2: Pressure (top) and flow rate (bottom) with time at the (left) aortic root (Root, segment 1) and midpoint of the aortic arch B (Arch, segment 14), thoracic aorta B (Tho, segment 27), and abdominal aorta D (Abd, segment 39), and (right) midpoint of the left common carotid (CCA, segment 15), left brachial (Bra, segment 21), right renal (Ren, segment 38) and left femoral (Fem, segment 46) arteries. They were simulated using a nonlinear visco-elastic 1-D model of pulse wave propagation in the larger 55 systemic arteries in the human (centre). The names and properties of these segments are shown in Table 1. The flow rate at the root (d) was measured *in vivo* and prescribed as the inflow boundary condition. In red, we show the uniform Windkessel pressure, p_w , given by Eq. (22), and Windkessel flow rate, $q_w = (p_w - P_{out})/R_T$, out of the arterial system into the microcirculation.

The vascular system has several features that make its mechanics difficult to model: its anatomy is complex, the flow is highly pulsatile, the blood vessels are generally very elastic and subject to cardiac and respiratory movements, and blood is a very complex fluid. But one of its most intriguing properties is its adaptability. There are a large number of control mechanisms that enable the cardiovascular system to adapt itself over a very wide range of conditions and time scales: from fast (jumping out of bed and running for the bus in the morning) to slow (growing up or adjusting to slow variation due to disease)⁵

One-dimensional (1-D) ‘reduced’ modelling⁶ is commonly applied to simulate the changes in

⁴For example, some vessels can be inaccessible to clinical measurements and several properties of interest are not directly measurable, can be dangerous to manipulate and can elicit reflex compensation *in vivo*.

⁵For example, arteries adapt their luminal diameter to maintain an approximately constant WSS [10]. Hypertension thickens the arterial wall to decrease circumferential stresses [11].

⁶Remarkably, the 1-D equations describing flow in elastic arteries, first published by Euler in 1775 [12], have the

blood flow and cross-sectionally averaged blood pressure and velocity in time and *only* along the axial direction of larger arteries⁷, with reasonable accuracy and computational cost⁸ [14, 15, 16]. For a historical overview of this field of research see [17] and the introductions in [18, 19, 20].

In this work we describe pulse wave mechanics in systemic arteries using mathematical and numerical tools based on the 1-D formulation in the time-domain, with a few references to the alternative Fourier-based frequency-domain approach [16, 21]. Section 2 introduces the 1-D formulation in the arterial network, including its assumptions, governing equations, characteristics analysis, numerical solution, and verification by comparison against *in vivo* and *in vitro* data. Section 3 shows important theoretical results on the physical mechanisms underlying the shape of the pressure and flow waveforms. Section 4 discusses tools based on the 1-D formulation to analyse *in vivo* pressure and flow waveforms in order to obtain clinically relevant properties of the cardiovascular system. We illustrate concepts using data generated in a 1-D model of the 55 larger systemic arteries in the human (Fig. 2, Section 2.8). The nomenclature and abbreviations used in this paper are listed in Tables 5 and 6 (Appendix 1).

2 Arterial one-dimensional formulation

We first introduce the governing equations of the arterial 1-D formulation and their main assumptions (Sections 2.1 to 2.3). We then analyse their solution using the method of characteristics (Section 2.4). We review several numerical schemes to solve the governing equations in Section 2.5, giving full details for our discontinuous Galerkin scheme. We describe the boundary conditions of the problem in Section 2.6. We review several tests that have been carried out to verify the accuracy of the 1-D formulation in Section 2.7 and conclude with a description of the 1-D model of the 55 larger systemic arteries shown in Fig. 2 (Section 2.8).

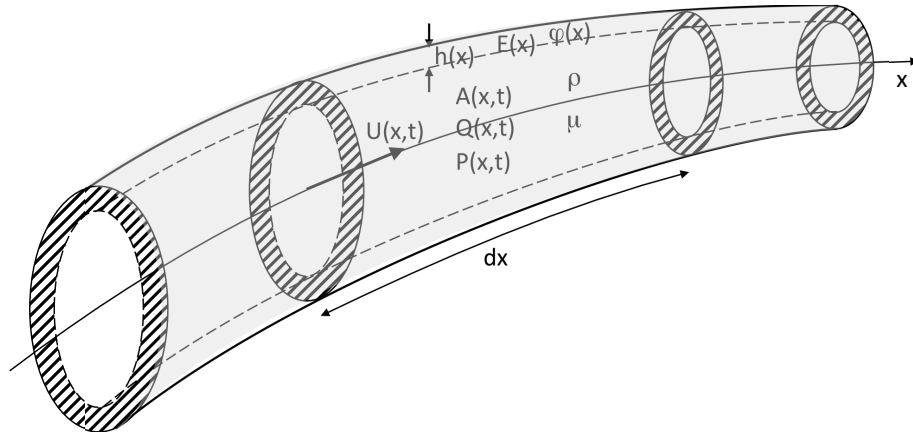


Figure 3: Layout of a 1-D compliant arterial segment (or domain Ω) whose properties are described by a single axial coordinate x . We denote the density and viscosity of blood by ρ and μ , respectively. At each cross section and for a time t , we denote the luminal area by $A(x,t)$, the wall thickness by $h(x)$, the wall Young's modulus by $E(x)$, the wall viscosity by $\varphi(x)$, the cross-sectional average velocity and pressure by $U(x,t)$ and $P(x,t)$, respectively, and the volume flux by $Q(x,t)$. The 1-D governing equations can be derived by applying conservation of mass and momentum to a differential control volume dx .

2.1 Assumptions and governing equations

In the 1-D formulation the arterial network is decomposed into arterial segments or domains Ω connected to each other at nodes. For example, we can decompose the systemic arterial tree in

same mathematical structure as the basic equations of compressible gas dynamics found in Lord Rayleigh's Theory of Sound (1894) [13]; the elasticity of the vessel wall taking the place of the compressibility of the gas.

⁷Research on venous 1-D modelling has received much less attention than arterial 1-D modelling.

⁸A 1-D simulation with the order of 100 arterial segments takes a few minutes to run on a normal PC.

Fig. 2 (centre) into 55 domains. Each domain is assumed to be a compliant tube whose properties can be described by a single axial coordinate x (Fig. 3).

The blood flow is assumed to be laminar, since Reynolds' numbers based on mean velocities are well below 2000 through most of the system in normal conditions [22]. In the ascending aorta, however, the flow can be highly disturbed during peak ejection, with peak Reynolds' numbers through the aortic valve close to 10 000 [23, 24]. Turbulence may also occur at other locations under some disease states such as luminal narrowing (*stenosis*) and abnormal aortic valves [24].

The pulse wave is assumed to propagate forward or backward in the x -direction (where positive x is taken as the direction of the mean blood flow). We also make use of the so-called *long wavelength approximation*, since pulse wavelengths are at least three orders of magnitude larger than arterial diameters and one order larger than the length of the longest arterial segments in Fig. 2 (centre)⁹. Pulse waves change the area of the luminal cross section $A(x, t) = \int_A d\sigma$; where t is the time and $d\sigma$ is a differential element of area. We also define the average velocity over the cross-section $U(x, t) = \frac{1}{A} \int_S \mathbf{u}(\mathbf{x}, t) \cdot \mathbf{n} d\sigma$, where \mathbf{x} is the three-dimensional (3-D) coordinate, \mathbf{u} is the velocity of each fluid particle in the cross-section A , and \mathbf{n} is the unit vector normal to A . The dependent variable $Q(x, t) = AU$ represents the volume flux at a given cross section.

Arteries are generally assumed to be tethered in the longitudinal direction, with their central axis fixed, and their wall allowed to deform only in the radial direction due to the internal pressure, denoted by $P(x, t)$, which is considered to be constant over the luminal cross-section A . This is consistent with the assumption that radial and azimuthal velocities are negligible compared to axial velocities, as shown in [25]. The external (or *extramural*) pressure is denoted by $P_{\text{ext}}(x, t)$ and the difference $P - P_{\text{ext}}$ is called the *transmural pressure*. The wall is usually assumed to be impermeable; only a few works account for the seepage of blood from the large arteries into the very small branches such as the *vasa vasorum* [26, 27].

Blood is a highly complex fluid comprising plasma (water, electrolytes and proteins) and flexible cells (predominantly red blood cells which occupy about 45% of the blood volume) with very complex rheological properties. At low shear rates, blood is non-Newtonian [1]. However, in large blood vessels, blood can be assumed to be a homogeneous, incompressible and Newtonian fluid¹⁰. [2]; blood viscosity, μ , and density, ρ , dependent only on temperature. Normal values at 37°C are $\rho = 1050 \text{ kg m}^{-3}$ and $\mu = 4.0 \text{ mPa s}$ [15]. Thus, we do not require a thermodynamic equation of state or an energy equation to formulate the problem. Analysis of the energy of the system, however, can provide valuable theoretical and numerical results for 1-D modelling [30, 31].

Gravitational effects are important in the distribution of blood volume, because of the effect of hydrostatic pressure on the deformable blood vessels. However, the effect is much larger in the thinner, more deformable veins, which contain up to 70% of the total blood volume, than in the thicker, less distensible arteries. Thus, gravitational effects are generally ignored or eliminated by considering only supine subjects in the study of arterial mechanics. Gravitational effects on arterial pulse wave propagation are studied in [32, 33, 34]. They are particularly important when studying the effect of postural changes [35] and simulating pulse wave propagation in veins [36, 37].

With these assumptions the 1-D governing equations follow from applying conservation of mass and momentum in a control volume of the 1-D vessel in Fig. 3 [19, 38],

$$\begin{cases} \frac{\partial A}{\partial t} + \frac{\partial Q}{\partial x} = 0 \\ \frac{\partial Q}{\partial t} + \frac{\partial}{\partial x} \left(\alpha \frac{Q^2}{A} \right) + \frac{A}{\rho} \frac{\partial P}{\partial x} = \frac{f}{\rho} \end{cases}, \quad (1)$$

where $f(x, t)$ is the frictional force per unit length and $\alpha(x, t) = \frac{1}{AU^2} \int_A \mathbf{u}^2 d\sigma$ is a non-dimensional

⁹In large arteries, pulse wave speeds are on the order of several metres per second. A typical resting heart rate of the order of one beat per second implies a wavelength of several metres.

¹⁰Non-Newtonian effects are studied in [28]. For an extensive overview on blood rheology or *haemorheology* see [29]

profile shape factor (sometimes called the *Coriolis coefficient*) that accounts for the non-linearity of the sectional integration of $\mathbf{u}(\mathbf{x}, t)$. Therefore, the velocity profile is required to close the system of equations, since it directly affects convective accelerations and the frictional term f .

In terms of the variables (A, U) (instead of (A, Q)) we have

$$\begin{cases} \frac{\partial A}{\partial t} + \frac{\partial(AU)}{\partial x} = 0 \\ \frac{\partial U}{\partial t} + (2\alpha - 1)U \frac{\partial U}{\partial x} + (\alpha - 1) \frac{U^2}{A} \frac{\partial A}{\partial x} + \frac{1}{\rho} \frac{\partial P}{\partial x} = \frac{f}{\rho A} \end{cases} \quad (2)$$

Eqs. (1) and (2) can also be derived by integrating the incompressible Navier–Stokes equations over a generic cross section of a cylindrical domain [14, 18, 25, 39, 40, 20]. Generalisation to curved vessels with arbitrary cross-sectional shapes relies upon a number of assumptions or restrictions. Probably the easiest approach is to require that pressure gradients in the cross-sectional plane are negligibly small.

2.2 Velocity profile and wall friction

The velocity profile changes in time and space and is not axisymmetric in areas of large curvature, such as the aortic arch. *In vivo* observations under normal conditions have shown that the mean profile in the aorta (*i.e.* the profile constructed from time-averaged measurements) is relatively blunt, with narrow boundary layers close to the wall and fluid outside the boundary layer travelling at a uniform velocity that is only slightly greater than the cross-sectional mean [23]. The profile is more parabolic in peripheral arteries [41], [2, Chap. 12].

In 1-D modelling the velocity profile is commonly assumed to be constant in shape and axisymmetric. A typical profile satisfying the no-slip condition ($u|_{r=\mathcal{R}} = 0$) is [18, 25]

$$u(x, r, t) = U \frac{\zeta + 2}{\zeta} \left[1 - \left(\frac{r}{\mathcal{R}} \right)^\zeta \right], \quad (3)$$

where r is the radial coordinate, $\mathcal{R}(x, t)$ is the radius of the lumen (assumed to be circular) and $\zeta = \frac{2-\alpha}{\alpha-1}$ is a constant. Eq. (3) can simulate profiles between close to flat flow ($\alpha \approx 1$) to parabolic flow ($\zeta = 2$). Following [25], $\zeta = 9$ ($\alpha = 1.1$) provides a good compromise fit to experimental data obtained at different points in the cardiac cycle. Boundary-layer type profiles have also been proposed [42].

Integration of the incompressible 3-D Navier-Stokes equations for axisymmetric vessels yields $f(x, t) = 2\mu\pi\mathcal{R} \left[\frac{\partial u}{\partial r} \right]_{r=\mathcal{R}}$ [25]. For the velocity profile given by Eq. (3) we have $f = -2(\zeta + 2)\mu\pi U$ in which the local f (and hence the WSS) is in phase with the flow¹¹. Several works [43, 44, 45, 46, 47] (and references therein) have included space- and time-varying axisymmetric velocity profiles in 1-D modelling, in which the local f is not in phase with the flow. According to [45], the effects of the velocity profile on the propagation of the arterial pulse are small. However, a more accurate simulation of the velocity profile enables the calculation of the WSS.

In the convective acceleration terms of Eqs. (1) and (2) the approximation $\alpha = 1$ is sometimes taken¹², which leads to considerable mathematical simplifications, especially with the treatment of the boundary conditions. Hereafter we will make use this approximation.

2.3 Pressure-area relationship

An explicit algebraic relationship between P and A (or *tube law*) is also required to close Eqs. (1) and (2) and account for the fluid-structure interaction of the problem. Mathematically we require

¹¹Note that $\zeta = 2$ ($\alpha = 4/3$) leads to Poiseuille flow resistance $f = -8\mu\pi U$.

¹²Note that for a velocity profile defined using Eq. (3) with $\zeta = 9$ we have $\alpha = 1.1$, which is close to one.

$P = \mathcal{A}(A(x, t); x, t)$, where the function \mathcal{A} depends on the model used to simulate the dynamics of the arterial wall.

Arterial walls are anisotropic and heterogeneous, composed of layers with different biomechanical properties whose stress–strain relationships are nonlinear and frequency dependent, and exhibit creep (continuous extension at constant load), stress relaxation (tension decay at constant length), and hysteresis (different stress–strain relationship for loading and unloading) [48, Chap. 8][49]. They contain smooth muscle, the proteins *elastin* and *collagen*, which are the main determinants of the elastic properties of the wall, and a small amount of *glycoproteins*, which are probably responsible for much of the viscous behaviour of the wall.

Elastin forms highly extensible elastic fibres and sheets, whereas collagen forms fibres that are about 1 000 times stiffer than elastin fibres [2]. In the unstretched configuration of an artery, collagen fibres are normally kinked and do not contribute significantly to the elastic properties of the wall. As pressure rises, an increasing number of collagen fibres reach their normal resting lengths and the arterial wall gets significantly stiffer. Smooth muscle cells contract and relax under neural and hormonal control (*vasomotor control*¹³) actively affecting arterial stiffness. They also play an important role in the visco-elastic damping of the pulse wave [50].

About half of the total systemic arterial compliance (the ability of the arterial system to distend with increasing blood pressure) is located upstream of the proximal thoracic aorta, which is the most elastic systemic artery [51]. Peripheral arteries are stiffer because they are more muscular, contain less elastin and more collagen and have a larger wall-thickness to diameter ratio. Their smooth muscle cells can change the luminal area (*vasomotion*) to regulate peripheral blood flow and satisfy the local instantaneous metabolic needs.

To define \mathcal{A} in 1-D modelling, the arterial wall is typically assumed to be thin, isotropic, homogeneous and incompressible, and to deform axisymmetrically with each cross section (which is assumed to be circular) independent of the others. Elastic and visco-elastic constitutive laws have been extensively used.

Voigt-type visco-elastic laws reproduce, to first approximation, the main features of visco-elastic effects on blood flow in large arteries, including hysteresis and creep [52, 53, 54, 55, 56, 57]. An example of this type of law that neglects the effects of wall inertia and longitudinal pre-stress (they are studied numerically in [58]) is given by [57]

$$P = P_e(A; x) + \frac{\Gamma(x)}{A_0(x)\sqrt{A}} \frac{\partial A}{\partial t}, \quad (4)$$

with

$$P_e(A, x) = P_{\text{ext}} + \frac{\beta(x)}{A_0(x)} \left(\sqrt{A} - \sqrt{A_0(x)} \right), \quad (5)$$

$$\beta(x) = \frac{4}{3}\sqrt{\pi}E(x)h(x), \quad \Gamma(x) = \frac{2}{3}\sqrt{\pi}\varphi(x)h(x),$$

where P_e is the elastic component of pressure, $h(x)$ is the wall thickness, $E(x)$ is the Young's modulus and $\varphi(x)$ is the wall viscosity, so that $\beta(x)$ is related to the wall elasticity and $\Gamma(x)$ to the wall viscosity; both being independent of the transmural pressure. The reference area $A_0(x)$ is the area when $P = P_{\text{ext}}$ and $\frac{\partial A}{\partial t} = 0$, which are typical initial conditions for numerical analysis. Therefore, the local cross-sectional area $A(x, t)$ will depend on the shape of the artery given by $A_0(x)$ and the mechanical properties of the wall, which may change with x ; *e.g.* the arterial wall becomes stiffer with the distance from the heart. More complex models also accounting for stress relaxation [59, 60, 61] and the nonlinear behaviour of the wall [47, 62] have been used.

2.4 Method of characteristics analysis

Under physiological conditions the elastic term in the tube law (4) is dominant over the viscous term. Neglecting the viscous term (*i.e.* taking $P = P_e$), Eqs. (2) and (5) form a system of

¹³Under normal conditions, the vasomotor control in the pulmonary arteries is believed to be much less important than in the systemic arteries [2].

hyperbolic partial differential equations that can be written in non-conservative form as

$$\frac{\partial \mathbf{U}}{\partial t} + \mathbf{H} \frac{\partial \mathbf{U}}{\partial x} = \mathbf{S}, \quad (6)$$

$$\mathbf{U} = \begin{bmatrix} A \\ U \end{bmatrix}, \quad \mathbf{H} = \begin{bmatrix} U & A \\ \frac{1}{\rho} \frac{\partial P_e}{\partial A} & U \end{bmatrix}, \quad \mathbf{S} = \begin{bmatrix} 0 \\ \frac{1}{\rho} \left(\frac{f}{A} - \frac{\partial P_{\text{ext}}}{\partial x} - \frac{\partial P_e}{\partial \beta} \frac{d\beta}{dx} - \frac{\partial P_e}{\partial A_0} \frac{dA_0}{dx} \right) \end{bmatrix}.$$

This system can be analysed using Riemann's method of characteristics. Since $A > 0$ and $\frac{1}{\rho} \frac{\partial P_e}{\partial A} > 0$ in normal physiological conditions, \mathbf{H} has two real and distinct eigenvalues, $\lambda_{f,b} = U \pm c$, where $c = \sqrt{\frac{A}{\rho} \frac{\partial P_e}{\partial A}}$ is the pulse wave speed of the system. Note that c and its relation to the density of blood, ρ , and the local distensibility of the artery, $\frac{1}{A} \frac{\partial A}{\partial P_e}$, is a result of the analysis, not a presumption. The matrix \mathbf{H} can be written as

$$\mathbf{H} = \mathbf{L}^{-1} \mathbf{\Lambda} \mathbf{L}, \quad \mathbf{L} = \delta \begin{bmatrix} \frac{c}{A} & 1 \\ -\frac{c}{A} & 1 \end{bmatrix}, \quad \mathbf{\Lambda} = \begin{bmatrix} \lambda_f & 0 \\ 0 & \lambda_b \end{bmatrix}, \quad (7)$$

with δ an arbitrary scaling factor. Substitution of (7) into (6) and premultiplication of (6) by \mathbf{L} yields

$$\mathbf{L} \frac{\partial \mathbf{U}}{\partial t} + \mathbf{\Lambda} \mathbf{L} \frac{\partial \mathbf{U}}{\partial x} = \mathbf{L} \mathbf{S}. \quad (8)$$

Taking $\frac{\partial \mathbf{W}}{\partial \mathbf{U}} = \mathbf{L}$, where $\mathbf{W} = [W_f, W_b]^T$ is the vector of characteristic (or Riemann) variables, Eq. (8) reduces to

$$\frac{\partial \mathbf{W}}{\partial t} + \mathbf{\Lambda} \frac{\partial \mathbf{W}}{\partial x} = \mathbf{L} \mathbf{S}. \quad (9)$$

For any path $x = \hat{x}(t)$ in the (x, t) space, the variation of \mathbf{W} along $\hat{x}(t)$ can be written as

$$\frac{d\mathbf{W}(\hat{x}(t), t)}{dt} = \frac{\partial \mathbf{W}}{\partial t} + \frac{d\hat{x}}{dt} \mathbf{I} \frac{\partial \mathbf{W}}{\partial x}. \quad (10)$$

Comparison of (9) and (10) shows that if the path $\hat{x}(t)$ is chosen such that $\frac{d\hat{x}}{dt} \mathbf{I} = \mathbf{\Lambda}$, then

$$\frac{d\mathbf{W}}{dt} = \mathbf{L} \mathbf{S} = \begin{bmatrix} \frac{1}{\rho} \left(\frac{f}{A} - \frac{\partial P_{\text{ext}}}{\partial x} - \frac{\partial P_e}{\partial \beta} \frac{d\beta}{dx} - \frac{\partial P_e}{\partial A_0} \frac{dA_0}{dx} \right) \\ \frac{1}{\rho} \left(\frac{f}{A} - \frac{\partial P_{\text{ext}}}{\partial x} - \frac{\partial P_e}{\partial \beta} \frac{d\beta}{dx} - \frac{\partial P_e}{\partial A_0} \frac{dA_0}{dx} \right) \end{bmatrix}. \quad (11)$$

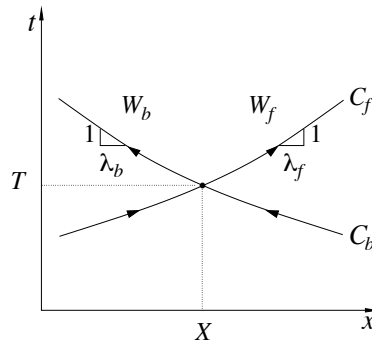


Figure 4: In the (x, t) space, every point (X, T) of a domain Ω is intersected by a unique pair of characteristic curves $C_f : \frac{d\hat{x}_f}{dt} = \lambda_f$ and $C_b : \frac{d\hat{x}_b}{dt} = \lambda_b$ along which the characteristic variables W_f and W_b propagate.

Thus, for any point (X, T) in the (x, t) space there are two characteristic paths, C_f and C_b , defined by $C_{f,b} \equiv \frac{d\hat{x}_{f,b}}{dt} = \lambda_{f,b} = U \pm c$, along which W_f and W_b propagate at speeds λ_f and λ_b , respectively (Fig. 4), changing their values due to fluid viscous dissipation and spatial variations of the external pressure, wall distensibility and reference luminal area. Under physiological flow

conditions, the local wave speed c is generally more than an order of magnitude greater than the maximum convective velocity U . Thus, $\lambda_f > 0$ and $\lambda_b < 0$ (*i.e.* the flow is subcritical¹⁴).

The characteristic variables W_f and W_b are then determined¹⁵ by integration of $\frac{\partial \mathbf{W}}{\partial \mathbf{U}} = \mathbf{L}$,

$$W_{f,b} = U - U_0 \pm 4(c - c_0), \quad (12)$$

with U_0 a reference blood velocity and

$$c = \sqrt{\frac{\beta}{2\rho A_0}} A^{1/4}, \quad c_0 = \sqrt{\frac{\beta}{2\rho}} A_0^{-1/4} = \sqrt{\frac{2Eh}{3\rho \mathcal{R}_0}}, \quad (13)$$

where c_0 and \mathcal{R}_0 are, respectively, the pulse wave speed and luminal radius at pressure P_{ext} .¹⁶ Note that c and c_0 increase with increasing elastic modulus and wall thickness and decreasing luminal area.

This analysis shows that W_f propagates changes in area (and, hence, pressure) and velocity in the positive x -direction of each arterial segment; *i.e.* forwards from *proximal* to *distal* parts in peripheral branches. On the other hand, W_b propagates changes in the negative x -direction; *i.e.* backwards from distal to proximal parts near the heart. Furthermore, if $f = 0$ and P_{ext} , β and A_0 are constant along x , then $\frac{d\mathbf{W}}{dt} = \mathbf{0}$, which implies that Eq. (9) is decoupled into two linear advection equations; *i.e.* W_f and W_b are constant along C_f and C_b , respectively. In this case, W_f and W_b are generally known as the *Riemann invariants*. Therefore, blood pressure and flow measured at any point in a compliant vessel may be described as the combination of forward- and backward-travelling waves.

The characteristic variables W_f and W_b are usually given by the boundary conditions (see Sections 2.6 and Appendix 2). However, in more complex cases in which changes are imposed upon the vessel (*e.g.* an external pressure applied on the vessel wall), W_f and W_b also depend on the conditions imposed everywhere along the vessel.

2.5 Numerical solution

The 1-D governing equations can be solved in a given network of arterial segments (*e.g.* those shown in Fig. 2, centre) using the method of characteristics [26, 66], finite element methods, such as Galerkin [67, 68, 46, 57] and Taylor-Galerkin (combined with operator splitting techniques) [58] schemes, and finite difference methods, such as the Lax-Wendroff method [42, 45] and the MacCormack method [56]. We solve Eqs. (2) and (4) using a discontinuous Galerkin scheme (see Appendix 2 for details).

2.6 Boundary conditions

Given that we have a convection-dominated problem with subcritical flow, we need to prescribe one boundary condition at both the inlet and outlet of each arterial segment Ω . We classify them into *inflow* (Section 2.6.1), *junction* (Section 2.6.2) and *terminal* (Section 2.6.3) boundary conditions. Appendix 2 shows how we prescribe them in our discontinuous Galerkin scheme.

2.6.1 Inflow boundary condition

This condition usually accounts for the flow at the inlet of the ascending aorta, the *aortic root* (Segment 1 in Fig. 2, centre), which is connected to the left ventricle of the heart through the

¹⁴The flow can be supercritical in stenosis [63].

¹⁵To satisfy the Cauchy-Riemann condition $\frac{\partial^2 W_{f,b}}{\partial A \partial U} = \frac{\partial^2 W_{f,b}}{\partial U \partial A}$ we must have a constant δ in \mathbf{L} (7). Without loss of generality we assume $\delta = 1$.

¹⁶Moens [64] and Korteweg [65] independently derived the equation $c = \sqrt{\frac{Eh}{2\rho \mathcal{R}_0}}$ for the pulse wave speed, which is similar to the equation for c_0 .

aortic valve. There, we usually prescribe the volume flow rate measured *in vivo*, $Q_{\text{in}}(t)$; an example is shown in Fig. 2 (bottom left). For each cardiac cycle, $Q_{\text{in}}(t)$ consists of a *systolic* and a *diastolic* phase, with the latter lasting about twice the time of the former under resting conditions. During *systole* the heart muscle contracts and blood is pumped into the aorta. At the end of systole the flow reverses shutting the aortic valve. This helps increase the flow toward the coronary arteries that branch off the aortic root to perfuse the heart¹⁷. During *diastole* the heart muscle relaxes and the left ventricle is refilled with blood.

In a healthy adult at rest, the *heart rate* is about 70 beats/min (bpm), giving a *cardiac period* of just less than 1 s. Each ventricle ejects about 70–100 mL of blood per stroke; the *stroke volume*. The net volume of blood ejected from the left ventricle to the ascending aorta per unit of time, the *cardiac output*, is around 6 l/min.¹⁸ During strenuous exercise it can increase to about 25 l/min.

More sophisticated boundary conditions at the aortic root have been developed to model the coupling between the left ventricle in the heart, the aortic valve and the arterial vasculature (the *ventricular-vascular coupling*); *e.g.* using lumped parameter models [71, 68, 47]. Some of these models include a 1-D representation of the larger coronary arteries.

2.6.2 Junction matching conditions

In the 1-D formulation the nodes connecting the arterial segments are treated as discontinuities, which is consistent with the long-wavelength approximation. Detailed 3-D calculations of flow at arterial bifurcations show that the flow is generally very complex with the possibility of transient separation and the development of secondary flows. Most of these flow features are confined to the region near the bifurcation and their effect on pulse wave propagation is commonly neglected in the 1-D formulation, again due to the long wavelength approximation.

Junction matching conditions allow us to connect individual arterial domains to form an arterial network. Here we will consider two types of junctions: (a) *splitting flow* (Fig. 5, left) and (b) *merging flow* (Fig. 5, right). In (a) the outlet of the parent vessel is connected to the inlets of the daughter vessels, whereas in (b) the inlet of the parent vessel is connected to the outlets of the daughter vessels.

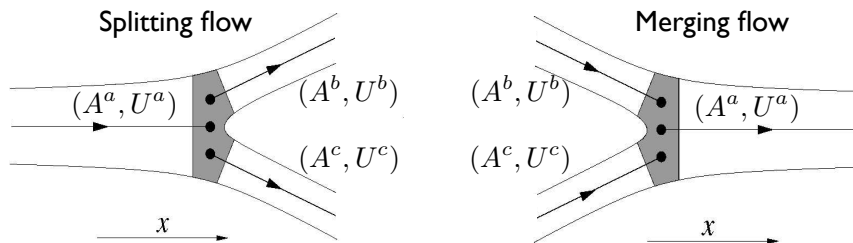


Figure 5: Nomenclature for the two types of junctions considered: splitting flow (left) and merging flow (right). The arrows indicate the positive direction of the axial coordinate x .

Splitting flow junctions are the most common arrangement in large human systemic arteries (Fig. 2, bottom left). Merging flow junctions allow us to simulate anastomosis which appear in more peripheral arteries, such as the circle of Willis in the cerebral circulation [72], the palmar arch in the hand [73] and the plantar arch in the foot. They are also important for modelling surgical interventions, such as arterial bypass grafting [67, 74]. Merging flow junctions are the most common arrangement in the venous system.

Energy losses at the junction are usually neglected, although some works have modelled them as a function of the flow rate and bifurcation angles [27, 58, 67, 75].

¹⁷An important feature of cardiac physiology is that, unlike other organs, the perfusion of the heart itself occurs predominately during *diastole*. This is because the contraction of the myocardium compresses the coronary blood vessels embedded within it, greatly increasing their resistance to flow [69, 70].

¹⁸Since the total blood volume in a normal adult is about 5 l, this means that the mean circulation time is less than a minute.

2.6.3 Terminal boundary conditions

Any arterial 1-D model has to be truncated after a relatively small number of generations of bifurcations, since 1-D model assumptions, such as blood being a continuum and Newtonian fluid, fail as the relative size of red blood cells to vessel diameter increases. In the most peripheral vessels (small arteries, arterioles and capillaries), fluid resistance dominates over wall compliance and fluid inertia, which are both dominant in large arteries.

The effect of peripheral resistance, compliance and fluid inertia on pulse wave propagation in large 1-D model arteries is commonly simulated using linear lumped parameter models (or zero-dimensional (0-D) models) coupled to the 1-D model terminal branches. Peripheral 0-D models are typically represented using electric circuits because of the analogy that exists between the linearised 1-D flow equations and the electric transmission line equations (see Section 3.1).

The RCR model shown in Fig. 13 (right) is a commonly used 0-D model. It consists of a resistance R_1 connected in series with a parallel combination of a second resistance R_2 and a compliance C ; P_{out} is the pressure at which flow to the microcirculation ceases¹⁹. This model relates pressure and the flow at the end point of a 1-D domain Ω through

$$Q \left(1 + \frac{R_1}{R_2} \right) + CR_1 \frac{\partial Q}{\partial t} = \frac{P_e - P_{\text{out}}}{R_2} + C \frac{\partial P_e}{\partial t}. \quad (14)$$

More sophisticated terminal models include 0-D models with time-dependent resistances to simulate flow control mechanisms [77], single tapering vessels [68] and structured-tree networks [78, 79] to capture some wave propagation phenomenon in downstream vessels, and 0-D (compartmental) models of the parts of the cardiovascular system that are not simulated using the 1-D formulation (*e.g.* the chambers of the heart and the venous circulation) [80, 81].

2.7 Tests using *in vivo* and *in vitro* data

The 1-D formulation has been satisfactorily tested by comparison with *in vivo* [82, 42, 67, 47, 83] and *in vitro* [84, 60, 75, 57, 56, 85] data in large systemic arteries. We have tested Eqs. (2) and (4) by comparison against *in vitro* data in a 1:1 replica of the 37 largest conduit arteries made of distensible silicone tubes (Fig. 6) [57]. The aorta is connected to a pump, which simulates the left ventricle, and the terminal branches are connected through resistance elements to a returning circuit, which simulates the venous return.

In this model we could accurately measure pressure and flow rate with time in the silicone network at over 70 locations and all the physical parameters required to run the 1-D model. Comparison of experimental and numerical waveforms (Fig. 6) shows the ability of the 1-D formulation to simulate pulse wave propagation in large arterial networks with reasonable accuracy.

However, the accuracy of the simulations relies on accurate measurements of all the model parameters, which is very challenging for patient-specific simulations. *In vivo*, we can obtain the geometry from medical images, such as CT, MR, 3D ultrasound (3DUS) and IVUS [87, 83], and vascular casts if we are working with animal models (Fig. 7). We can also measure the flow at the ascending aorta (using either magnetic resonance imaging [88] or ultrasound [89, p. 38]) and prescribe it as the inflow boundary condition, $Q_{\text{in}}(t)$. For the rest of parameters we can use the 1-D formulation to find analytical relationships between them and data that can be measured *in vivo* (see Section 4), based on a theoretical understanding of the physical mechanisms underlying the shape of the pulse waveform (see Section 3). We will first describe the model that we use here to illustrate the results described in Sections 3 and 4.

2.8 Model of the 55 larger systemic arteries in the human

We solve the nonlinear 1-D equations (2) and (4) in the 55 larger arteries in the human (Fig. 2, centre). Tables 1 and 2 show their properties, which are based on data in young and healthy humans

¹⁹In general, P_{out} is much larger than the venous pressure due to waterfall effects [76].

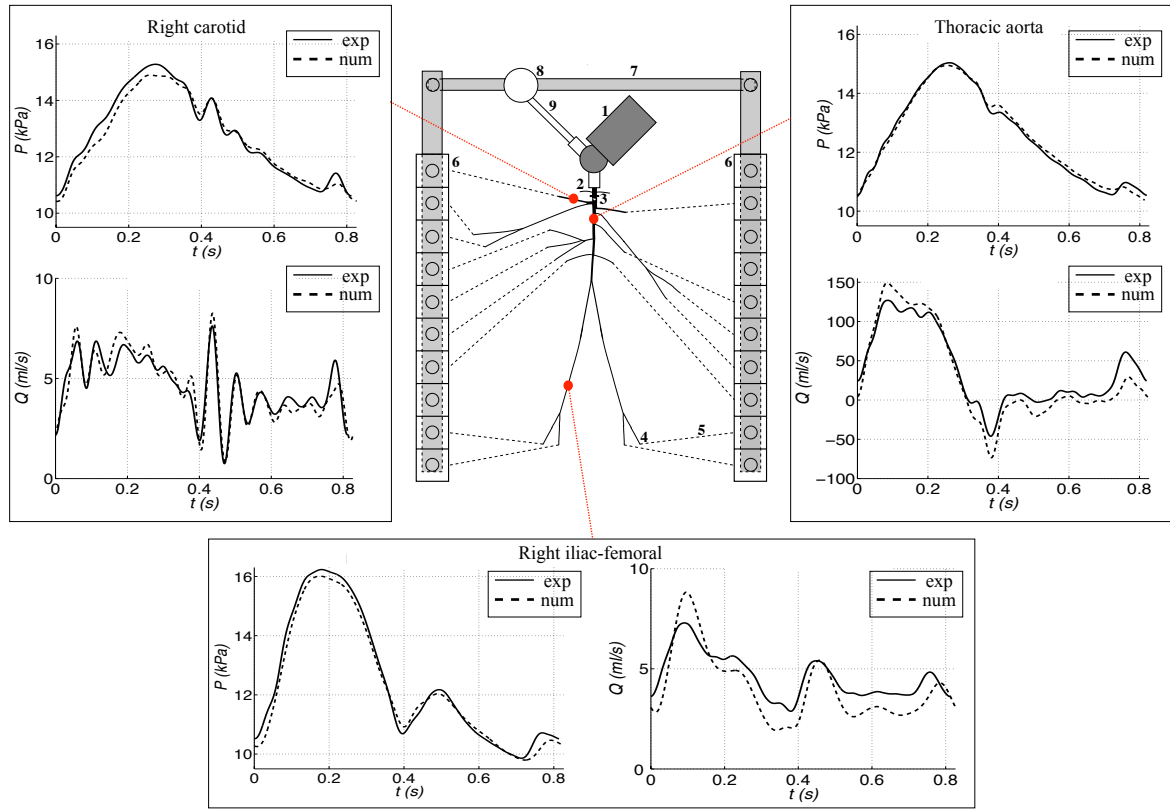


Figure 6: Experimental (exp) and simulated (num) pressure and flow waveforms in the right carotid artery (left), thoracic aorta (right) and right femoral artery (bottom) of a 1:1 replica of the 37 largest systemic arteries (top middle). 1: Pump (left heart); 2: catheter access; 3: aortic valve; 4: peripheral resistance tube; 5: stiff plastic tubing (veins); 6: venous overflow; 7: venous return conduit; 8: buffering reservoir; 9: pulmonary veins. Note the different scales of flow rates. (Modified from [57].)

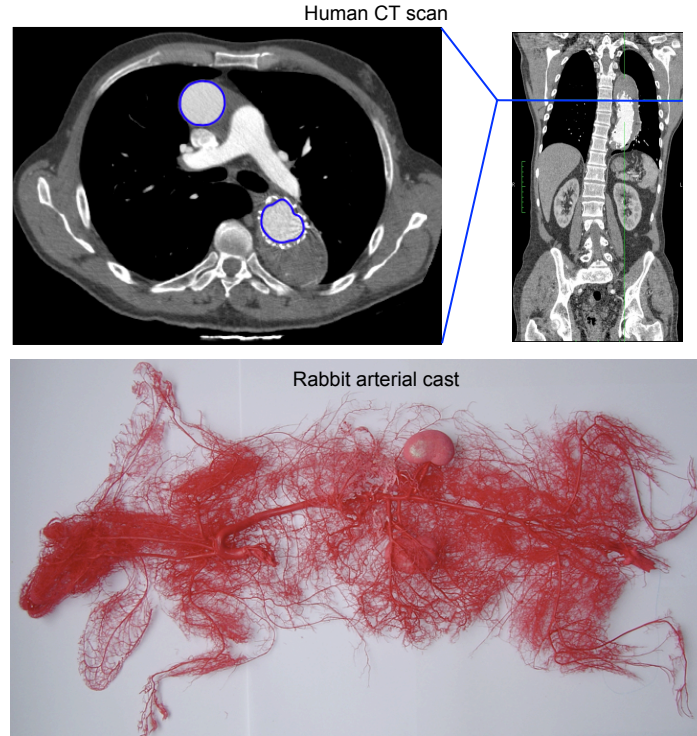


Figure 7: (top) Frontal (or coronal) view (right) and transversal slice (left) of a human thorax obtained using a CT scanner. The aortic lumen is highlighted in blue on the transversal slide. (right) Cast of the systemic circulation of a male New Zealand white rabbit. (Modified from [86].)

Table 1: Parameters of the arterial tree in Model 1 (Fig. 2, centre). $\mathcal{R}_{\text{in}} \rightarrow \mathcal{R}_{\text{out}}$: mean cross-sectional radii at the inlet and outlet of the arterial segment (radii decrease linearly); $c_{\text{in}} \rightarrow c_{\text{out}}$: mean wave speed at the inlet and outlet of the segment. Mean pressures and flows calculated in the midpoint of the segment. The wall viscosity φ is 0.5 kPa s in Segments 1, 2, 14, 18, 26–30, 35, 37, 39 and 41; 1.0 kPa s in Segments 3, 4, 19, 34, 42 and 43; 2.5 kPa s in Segments 7, 21, 31, 36, 38, 40, 44 and 50; and 6.0 kPa s in Segments 5, 6, 8, 9–13, 15–17, 20, 22–25, 32, 33, 45–49, and 51–55. The outflow pressure is 1.33 kPa (10 mmHg) at each terminal branch.

Arterial segment name	Length (cm)	$\mathcal{R}_{\text{in}} \rightarrow \mathcal{R}_{\text{out}}$ (mm)	$c_{\text{in}} \rightarrow c_{\text{out}}$ (m s ⁻¹)	Mean pressure (mmHg)	Mean flow (mL s ⁻¹)	Peripheral resistance (mmHg s mL ⁻¹)	Peripheral compliance (10 ⁻² mL mmHg ⁻¹)
1. Ascending aorta	5.8	15.4 → 15.4	4.0 → 4.0	100.1	102.8	-	-
2. Aortic arch A	2.3	13.2 → 12.6	4.2 → 4.2	100.0	89.3	-	-
3. Brachiocephalic	3.9	10.6 → 9.4	4.5 → 4.6	99.9	13.5	-	-
4. R. subclavian	3.9	6.0 → 4.7	5.3 → 5.7	99.9	7.0	-	-
5. R. common carotid	10.8	5.7 → 2.9	5.3 → 6.5	99.7	6.5	-	-
6. R. vertebral	17.1	1.9 → 1.4	8.1 → 8.7	89.9	2.3	33.8	1.20
7. R. brachial	48.5	4.2 → 2.4	6.4 → 7.5	95.1	4.7	-	-
8. R. radial	27.0	1.9 → 1.6	8.0 → 8.4	81.2	2.4	29.7	1.32
9. R. ulnar A	7.7	1.9 → 1.7	8.0 → 8.2	91.9	2.3	-	-
10. R. interosseous	9.1	1.1 → 0.9	9.5 → 10.0	89.2	0.2	474.2	0.43
11. R. ulnar B	19.7	1.6 → 1.4	8.4 → 8.7	75.6	2.2	29.7	1.03
12. R. internal carotid	20.5	2.9 → 2.2	7.1 → 7.7	92.2	5.8	14.1	3.45
13. R. external carotid	18.7	1.3 → 0.8	9.1 → 10.4	71.5	0.7	78.2	2.57
14. Aortic arch B	4.5	11.2 → 10.9	4.4 → 4.4	99.6	83.8	-	-
15. L. common carotid	16.0	5.1 → 2.5	5.5 → 6.8	98.9	5.5	-	-
16. L. internal carotid	20.5	2.2 → 1.7	7.7 → 8.2	83.3	5.1	14.1	2.52
17. L. external carotid	18.7	1.0 → 0.6	9.8 → 11.1	54.1	0.5	78.2	2.31
18. Thoracic aorta A	6.0	10.4 → 9.9	4.5 → 4.6	99.4	76.5	-	-
19. L. subclavian	3.9	5.7 → 4.4	5.3 → 5.8	105.4	7.2	-	-
20. L. vertebral	17.0	1.9 → 1.4	8.1 → 8.7	89.9	2.3	33.8	1.20
21. L. brachial	48.5	4.2 → 2.4	6.4 → 7.5	94.8	4.9	-	-
22. L. radial	27.0	1.8 → 1.4	8.2 → 8.7	76.9	2.2	29.7	1.13
23. L. ulnar A	7.7	2.2 → 2.2	7.7 → 7.7	93.0	2.7	-	-
24. L. interosseous	9.1	0.9 → 0.9	10.0 → 10.0	89.6	0.2	474.2	0.37
25. L. ulnar B	19.7	2.1 → 1.9	7.8 → 8.0	86.6	2.6	29.7	1.73
26. Intercostals	9.2	6.6 → 4.9	5.1 → 5.6	99.2	2.0	45	13.9
27. Thoracic aorta B	12.0	8.6 → 6.7	4.7 → 5.1	97.9	74.5	-	-
28. Abdominal aorta A	6.1	6.3 → 6.3	5.2 → 5.2	97.5	61.3	-	-
29. Celiac A	2.3	4.1 → 3.6	5.9 → 6.1	97.9	13.2	-	-
30. Celiac B	2.3	2.7 → 2.5	6.7 → 6.8	97.8	8.9	-	-
31. Hepatic	7.6	2.8 → 2.3	7.2 → 7.6	97.3	4.3	20.4	2.73
32. Gastric	8.2	1.6 → 1.5	8.4 → 8.5	91.7	2.6	30.4	1.09
33. Splenic	7.2	2.2 → 2.0	7.7 → 7.9	93.4	6.3	13.1	1.87
34. Superior mesenteric	6.8	4.1 → 3.7	5.9 → 6.1	97.5	16.7	5.2	6.41
35. Abdominal aorta B	2.3	6.0 → 5.9	5.3 → 5.3	97.5	44.6	-	-
36. L. renal	3.7	2.7 → 2.7	6.7 → 6.7	95.8	13.4	6.4	3.08
37. Abdominal aorta C	2.3	6.1 → 6.1	5.2 → 5.2	97.4	31.2	-	-
38. R. renal	3.7	2.7 → 2.7	6.7 → 6.7	95.4	13.4	6.4	3.08
39. Abdominal aorta D	12.2	6.0 → 5.7	5.3 → 5.3	97.2	17.8	-	-
40. Inferior mesenteric	5.8	2.4 → 1.6	7.5 → 8.4	96.9	2.2	38.7	1.78
41. Abdominal aorta E	2.3	5.6 → 5.4	5.4 → 5.4	97.1	15.6	-	-
42. L. common iliac	6.8	4.1 → 3.6	5.9 → 6.1	96.9	7.8	-	-
43. R. common iliac	6.8	4.1 → 3.6	5.9 → 6.1	96.9	7.8	-	-
44. L. external iliac	16.6	3.3 → 3.1	6.3 → 6.3	95.4	5.9	-	-
45. L. internal iliac	5.8	2.1 → 2.1	7.9 → 7.9	95.9	1.9	44.7	1.82
46. L. femoral	50.9	2.7 → 1.9	7.3 → 7.9	84.9	2.9	-	-
47. L. deep femoral	14.5	2.1 → 1.9	7.9 → 8.0	90.2	3.0	26.8	1.69
48. L. posterior tibial	36.9	1.6 → 1.4	8.4 → 8.6	58.3	1.8	26.8	0.99
49. L. anterior tibial	39.8	1.3 → 1.1	8.9 → 9.1	45.6	1.1	31.4	0.68
50. R. external iliac	16.6	3.3 → 3.1	6.3 → 6.3	95.4	5.9	-	-
51. R. internal iliac	5.8	2.1 → 2.1	7.9 → 7.9	95.9	1.9	44.7	1.82
52. R. femoral	50.9	2.7 → 1.9	7.3 → 7.9	84.9	2.9	-	-
53. R. deep femoral	14.5	2.1 → 1.9	7.9 → 8.0	90.2	3.0	26.8	1.69
54. R. posterior tibial	36.9	1.6 → 1.4	8.4 → 8.6	58.3	1.8	26.8	0.99
55. R. anterior tibial	39.8	1.3 → 1.1	8.9 → 9.1	45.6	1.1	31.4	0.68

[90, 53, 47]. We prescribe the periodic flow rate shown in Fig. 2 (bottom left) as the boundary condition at the inlet of the ascending aorta (Segment 1) and couple RCR models to each terminal branch. We divide arterial segments into non-overlapping elements with a 2 cm length and a poly-

Table 2: Reflection coefficients at the arterial junctions of Model 1 for a wave coming from the parent vessel (R_f^a), the daughter vessel I (R_f^b) and the daughter vessel II (R_f^c). They are calculated using Eq. (19) with mean (time-averaged) radii and wave speeds. The last column indicates the ratio of the sum of the two daughter mean areas to the parent mean area.

Parent—Daughter I—Daughter II	R_f^a	R_f^b	R_f^c	Area ratio
1—2—3	-0.06	-0.34	-0.60	1.2
2—14—15	0.06	-0.19	-0.87	1.0
3—4—5	0.20	-0.58	-0.62	0.8
4—6—7	0.09	-0.87	-0.22	1.0
5—12—13	-0.03	-0.11	-0.87	1.2
7—8—9	-0.07	-0.46	-0.46	1.2
9—10—11	-0.09	-0.70	-0.21	1.3
14—18—19	-0.07	-0.15	-0.79	1.2
15—16—17	0.11	-0.23	-0.88	0.9
18—26—27	-0.06	-0.63	-0.31	1.2
19—20—21	0.02	-0.86	-0.16	1.1
21—22—23	-0.14	-0.56	-0.30	1.4
23—24—25	-0.01	-0.87	-0.12	1.1
27—28—29	-0.09	-0.20	-0.71	1.3
28—34—35	-0.11	-0.67	-0.22	1.3
29—30—31	-0.02	-0.49	-0.49	1.2
30—32—33	0.01	-0.65	-0.35	1.2
35—36—37	-0.12	-0.85	-0.03	1.3
37—38—39	-0.05	-0.86	-0.09	1.2
39—40—41	-0.04	-0.88	-0.08	1.1
41—42—43	-0.03	-0.49	-0.49	1.2
42—44—45	-0.03	-0.21	-0.76	1.2
43—50—51	-0.03	-0.21	-0.76	1.2
44—46—47	0.01	-0.36	-0.65	1.2
46—48—49	-0.02	-0.39	-0.59	1.1
50—52—53	0.01	-0.36	-0.65	1.2
52—54—55	-0.02	-0.39	-0.59	1.1

Table 3: Comparison of simulated haemodynamic quantities at the aortic root with their corresponding values measured *in vivo* in the supine position (first four rows). SP: systolic pressure; MP: mean pressure; DP: diastolic pressure; HR: heart rate; CO: cardiac output; SV: stroke volume; AR: aortic radius.

	SP (mmHg)	MP (mmHg)	DP (mmHg)	HR (bpm)	CO (L min ⁻¹)	SV (mL)	C_T (mL mmHg ⁻¹)	AR (cm)
Normal [90]	—	—	—	72 ± 3	6.9 ± 0.4	96 ± 10	2.27 ± 0.07	—
Hypertensive [90]	—	—	—	72 ± 3	6.6 ± 0.3	92 ± 8	1.61 ± 0.04	—
Type C [91]	116 ± 7	99 ± 5	80 ± 4	80 ± 5	7.5 ± 0.3	95 ± 6	—	1.2 ± 0.1
Mean [91]	117 ± 3	96 ± 2	77 ± 2	76 ± 3	6.9 ± 0.2	92 ± 3	—	1.2 ± 0.03
Mean [92]	—	91 ± 8	—	69 ± 6	6.5 ± 0.8	—	—	—
Model $M1$	119.4	99.8	79.0	63	6.17	98.2	1.68 [†]	1.5 [‡]
Model $M2$	141.0	99.8	61.8	63	6.17	98.2	0.93 [†]	1.5 [‡]
Model $M3$	150.9	131.5	110.7	63	6.17	98.2	1.71 [†]	1.5 [‡]
Model $M4$	171.3	131.7	93.5	63	6.17	98.2	0.98 [†]	1.5 [‡]

[†] $C_T = C_c + C_p$ is calculated using Eq. (23) with time-averaged radii and wave speeds and $C_{0D}^i = \int_0^{l^i} C_{1D}^i dx$ to account for the changes of C_{1D}^i with x in our models due to tapering.

[‡] Mean value over one cardiac cycle.

nomial order of 3. Elements or segments shorter than 1.5 cm are given a polynomial order of 2.

Figure 2 shows the simulated pressure and flow with time in several arterial segments. They exhibit the following characteristic features observed *in vivo* under normal conditions. Pressure evolves between a maximum value, the *systolic pressure*, and a minimum value, the *diastolic pressure*. Their difference (the *pulse pressure*) tends to increase in the aorta as we move away from

Table 4: Comparison of simulated haemodynamic quantities in the midpoint of the left and right (between brackets) brachial arteries (Segments 7 and 21, respectively) with their corresponding values measured *in vivo* in the supine position (first two rows). SP: systolic pressure; MP: mean pressure; DP: diastolic pressure; HR: heart rate.

	Age (year)	SP (mmHg)	MP (mmHg)	DP (mmHg)	HR (bpm)
Normal [90]	37 ± 2	126 ± 3	90.7 ± 11	71 ± 3	72 ± 3
Hypertensive [†] [90]	39 ± 1	181 ± 4	132.4 ± 11	100 ± 2	72 ± 3
Model <i>M1</i>	15 – 30	128.4 (129.1)	98.5 (98.6)	75.9 (76.2)	63
Model <i>M2</i>	15 – 30	145.3 (144.4)	98.4 (98.6)	59.4 (59.6)	63
Model <i>M3</i>	15 – 30	159.8 (160.6)	130.1 (130.3)	107.2 (107.5)	63
Model <i>M4</i>	15 – 30	175.5 (174.7)	130.3 (130.4)	90.7 (90.9)	63

[†]Patients were considered to be hypertensive if DP \geq 90 mmHg.

the heart, whereas mean pressure gradually decreases²⁰ [41, 2] due to the cumulative effect of wall friction. At the ascending aorta, the systolic ejection yields a sudden rise in pressure followed by a sharp drop. A second smaller pressure peak is observed at the start of diastole, which forms the *dicrotic notch*, followed by a much smoother pressure decrease. The dicrotic notch vanishes in the aorta somewhere in the thoracic region (Fig. 1), but is observed in other proximal arteries such as the common carotid [62] and coronary [69] arteries. Moreover, the initial pressure increase becomes steeper and narrower in time in more peripheral locations (*wave steepening*) [41] and a pressure wide peak appears from the abdominal aorta to the leg arteries [41] and in the brachial artery [90]. The area–pressure curve exhibits hysteresis (Fig. 8a) due to wall visco-elasticity.

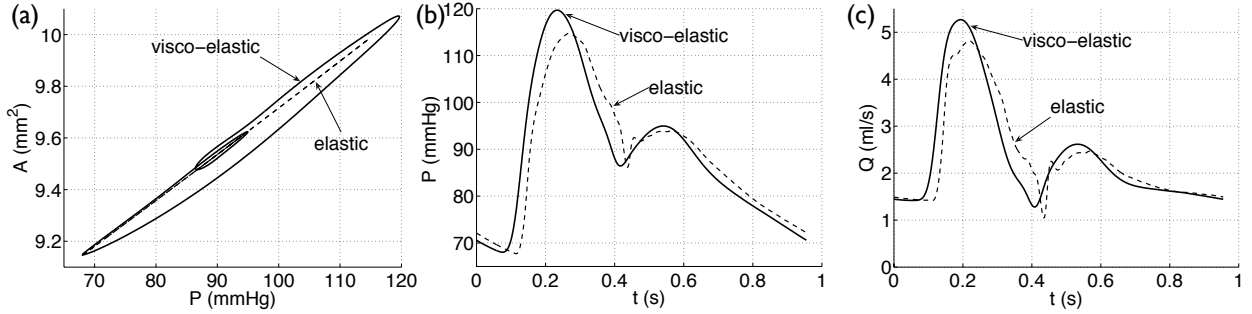


Figure 8: Simulated area–pressure curve (a), pressure with time (b) and flow rate with time (c) in the midpoint of the right radial artery of the 55-artery *normal young* model (Segment 12). Visco-elastic and purely-elastic results are compared.

As we move away from the heart, the flow waveform is characterised by an increase in width, a decrease in reversed flow, and a reduction in amplitude and mean value because of flow division at branching sites. Reversed flow is typically absent in the suprarenal region of the aorta [47] and carotid arteries, where the flow is called *antegrade* (unidirectional toward the head)²¹ [72, 93]. There is, however, a region of reversed flow in early diastole in the infrarenal region of the aorta and leg arteries [94].

Pressure and velocity waveforms are altered by ageing [95], hypertension [96], vascular disease [97], postural changes [35], pharmacological interventions [96, 98] and clinical maneuvers [92]. We can use the 1-D formulation to study physical mechanisms underlying these alterations, which we illustrate using three variations of the 55-artery model described above (hereinafter referred to as *Model M1*; *normal young*):

- *Model M2*; *normal old*: The elastic modulus E is increased three-fold in all the arterial

²⁰This is difficult to observe in Fig. 2 since the decrease in mean pressure is small compared to the pulse pressure.

²¹In normal conditions, the internal carotid and renal arteries have smaller peripheral vascular resistances than other arteries of similar calibre, such as the ulnar and femoral arteries.

segments except for the terminal branches.²²

- *Model M3; hypertensive young*: The total resistance $R_1 + R_2$ at the outflow of each 1-D model terminal branch (Fig. 13, right) is increased by 40%. The initial areas $A_0(x)$ are calculated using Eq. (30) with a reference pressure $P_{\text{ref}} = 130$ mmHg that is 40% greater than in M1.
- *Model M4; hypertensive old*: It combines the changes introduced in M2 and M3.

Tables 3 and 4 compare general haemodynamic data produced by the different models with the corresponding values measured *in vivo* in normal patients [90, 91, 92].

3 Linear analysis of the 1-D formulation

To further analyse the mechanisms underlying the shape of the pressure and flow waveforms we can linearise Eqs. (1) and (4) about the reference state $(A, P, P_e, Q) = (A_0, 0, 0, 0)$, with β , A_0 and Γ constant along x , which yields

$$\begin{cases} C_{1D} \frac{\partial p_e}{\partial t} + \frac{\partial q}{\partial x} = 0, \\ L_{1D} \frac{\partial q}{\partial t} + \frac{\partial p_e}{\partial x} - \gamma \frac{\partial^2 q}{\partial x^2} = -R_{1D} q, \\ p = p_e - \gamma \frac{\partial q}{\partial x}, \quad p_e = \frac{a}{C_{1D}}, \quad \gamma = \frac{\Gamma}{A_0^{3/2}}, \end{cases} \quad (15)$$

where a , p , p_e and q are the perturbation variables for area, pressure, elastic component of pressure, and flow rate, respectively, *i.e.* $(A, P, P_e, Q) = (A_0 + a, p, p_e, q)$, and

$$C_{1D} = \frac{2A_0^{3/2}}{\beta}, \quad L_{1D} = \frac{\rho}{A_0}, \quad R_{1D} = \frac{2(\zeta + 2)\pi\mu}{A_0^2} \quad (16)$$

are the elastic wall compliance, fluid inertia and viscous resistance (due to blood viscosity), respectively, per unit length of vessel.

These equations allow us to study *local* effects of the parameters of an arterial segment on the pulse waveform (Section 3.1), reflected waves at arterial junctions, terminal branches and aortic valve (Section 3.2), and *global* effects involving the arterial network as a whole (Section 3.3).

3.1 Waveforms in a single arterial segment

The method of characteristics (Section 2.4) applied to Eqs. (15) with zero fluid and wall viscosity ($\mu = \gamma = 0$), shows that linear changes in pressure, $p_e(x, t)$, and flow, $q(x, t)$, are propagated in straight characteristic lines; forward by w_f at a speed c_0 and backward by w_b at a speed $-c_0$, with

$$w_{f,b} = q \pm \frac{p_e}{Z_0}, \quad Z_0 = \frac{\rho c_0}{A_0}, \quad c_0 = \sqrt{1/(C_{1D} L_{1D})}. \quad (17)$$

The variables w_f and w_b are the linear Riemann variables and Z_0 is the *characteristic impedance*²³ of the vessel.²⁴ For waves propagating only in the forward direction we have $w_b = 0$ and, hence, $p_e = Z_0 q$; for waves propagating only in the backward direction, $w_f = 0$ yields $p_e = -Z_0 q$. Thus,

²²With age, E increases due to a loss of elastin and earlier engagement of collagen fibres with pressure increases.

²³In the mammalian systemic circulation, the aortic Z_0 is about 5-7% of the peripheral resistance R_T introduced by Eq. (21) [99].

²⁴Equations (17) are the linear form of the *water hammer* equations. For the nonlinear system they are $dP_{f,b} = \pm \rho c dU_{f,b}$ [100].

the stiffer the vessel is the faster the pulse wave propagates and, in a vessel without any wave reflection, the greater the pressure amplitude is for a given flow amplitude.

Fourier analysis allows us to study the effect of fluid and wall viscosity on pulse wave propagation. If $L_{1D} > \gamma C_{1D} R_{1D}$ (*i.e.* fluid inertia dominates over the combined effect of wall compliance and fluid and wall viscous damping), which is equivalent to $\rho E A_0 > 2(\zeta + 2)\pi\varphi\mu$, then the amplitude of the pressure and flow waves decays exponentially with distance x [101]. This is satisfied for the aorta in normal conditions, since $\rho E A_0$ is two orders of magnitude greater than $2(\zeta + 2)\pi\varphi\mu$. It is usually satisfied for arteries with smaller diameter, since the decrease in A_0 is counterbalanced by the increase in the Young's modulus E and the decrease in the velocity profile constant ζ . Indeed, peripheral arteries are stiffer than the aorta [2, Chap. 7] and have a velocity profile closer to parabolic [79].

The visco-elastic damping (or attenuation²⁵) with distance is greater with the increasing frequency of the wave, blood viscosity, μ , and wall viscosity, φ , and the decreasing Young's modulus, E , and arterial cross-sectional area, A_0 . At low frequencies the damping due to μ is dominant, whereas at higher frequencies the damping due to φ dominates [103, 101].

Consistent with these results, blood viscosity decreases the magnitude of the pressure waveform with distance in the 55-artery model, without significantly modifying its shape, whereas wall viscosity smoothes the high-frequency components of both the pressure and flow waveforms (Fig. 8b,c), specially in peripheral branches [104, 47, 101]. This smoothing mechanism is responsible for the progressive disappearance of the dicrotic notch with the distance from the heart²⁶.

Wall viscosity also causes wave dispersion; *i.e.* higher-frequency waves travel faster than lower-frequency ones. This leads to an earlier arrival of the feet of the pressure and flow waveforms (Fig. 8b,c). Another visco-elastic effect is the amplification of the pulse pressure in early systole, due to the expansion of the vessel wall ($\partial A/\partial t > 0$) (Fig. 8b), which is in agreement with Eq. (4). The opposite effect is observed when the vessel wall relaxes ($\partial A/\partial t < 0$) in late systole and diastole.

System (15) can be further simplified by integration over the length, l , of an arterial domain $\Omega \in [0, l]$, which yields

$$\begin{cases} C_{0D} \frac{d\tilde{p}_e}{dt} + q_{out} - q_{in} = 0 \\ L_{0D} \frac{d\tilde{q}}{dt} + p_{e_{out}} - p_{e_{in}} - \gamma \left(\frac{\partial q_{out}}{\partial x} - \frac{\partial q_{in}}{\partial x} \right) = -R_{0D} \tilde{q} \end{cases}, \quad (18)$$

where

$$\begin{aligned} q_{in}(t) &= q(0, t), & p_{e_{in}}(t) &= p_e(0, t), & \frac{\partial q_{in}}{\partial x}(t) &= \frac{\partial q}{\partial x}(0, t), \\ q_{out}(t) &= q(l, t), & p_{e_{out}}(t) &= p_e(l, t), & \frac{\partial q_{out}}{\partial x}(t) &= \frac{\partial q}{\partial x}(l, t), \end{aligned}$$

$R_{0D} = R_{1D}l$, $L_{0D} = L_{1D}l$, and $C_{0D} = C_{1D}l$. The space-averaged elastic pressure and flow rate over the arterial segment are given, respectively, by $\tilde{p}_e(t) = \frac{1}{l} \int_0^l p_e dx$ and $\tilde{q}(t) = \frac{1}{l} \int_0^l q dx$.

Neglecting wall viscosity and assuming $\tilde{p}_e = p_{in}$ and $\tilde{q} = q_{out}$ ²⁷ a finite number N of 0-D systems governed by Eq. (18), each with length $\Delta x = l/N$, discretise, at first-order accuracy in space, a linear continuous 1-D model arterial segment of length l governed by Eq. (15) [105]. The resulting system is analogous to the electric transmission line equations, in which the role of the flow and pressure are played by the electric current and potential, respectively, the total fluid resistance of the segment, R_{0D} , corresponds to an electric resistance, the total fluid inertia, L_{0D} , is equivalent to

²⁵Methods for the measurement and analysis of wave attenuation in the presence of reflections are discussed in [102].

²⁶The dicrotic notch is present in the abdominal aorta of the *normal young* model if wall viscosity is neglected.

²⁷Because of the long wavelength approximation, the entire arterial segment is assumed to pulse in synchrony, except for the outlet pressure and inlet flow, which are changed by the wall compliance, fluid inertia and wall resistance.

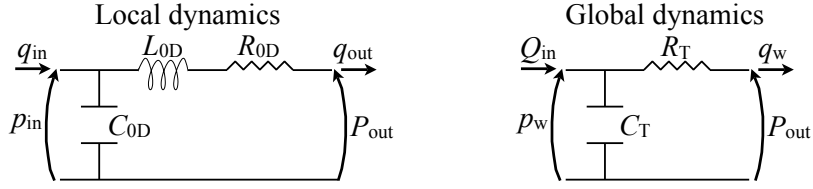


Figure 9: (left) A finite number of this 0-D electric analogous model governed by Eq. (18) discretises, at first-order accuracy in space, a linear continuous 1-D model arterial segment of length l governed by Eq. (15) [105]. (right) The pressure $p_w(t)$ dictated by this analog electric circuit provides a 0-D order approximation to the pressure waveform that is particularly accurate during diastole.

an inductance, and the total arterial compliance, C_{0D} , is matched by a capacitance (Fig. 9, left). Based on this linear approach, numerical [104, 106, 107, 108] and electric analog [109] models have been produced to simulate pulse wave propagation in the systemic arterial tree.

Zero-dimensional models are also used to simulate the entire circulatory system as a collection of compartments, in which the systemic arterial circulation can be represented as a single 0-D compartment. These models allow us to study (simplified) haemodynamics in the entire circulatory system and the hydraulic load on the isolated heart and cardiac assisted devices [110, 111, 112, 21].

3.2 Wave reflections

The linearised system of governing equations yields an analytical solution for wave reflection and transmission at points where the physical properties of the arteries change. At a splitting and merging flow junction (Fig. 5), the reflection coefficients for waves propagating in the parent, R_f^a , and two daughter, R_f^b and R_f^c , vessels can be defined as the ratio of the change of pressure (or area) across the reflected wave to the change of pressure (or area) in the incident wave. (Hereinafter, the superscripts a , b and c will be used to refer to the parent and first and second daughter vessels, respectively.) They can be expressed as a function of the *characteristic admittance* of each segment, $Y_0^j = 1/Z_0^j = \rho c^j/A_0^j$, $j = a, b, c$ (see Appendix 3),

$$R_f^a = \frac{Y_0^a - Y_0^b - Y_0^c}{Y_0^a + Y_0^b + Y_0^c}, \quad R_f^b = \frac{Y_0^b - Y_0^c - Y_0^a}{Y_0^a + Y_0^b + Y_0^c}, \quad R_f^c = \frac{Y_0^c - Y_0^a - Y_0^b}{Y_0^a + Y_0^b + Y_0^c}. \quad (19)$$

The transmission coefficients for waves propagating in the parent, T^a , and two daughter, T^b and T^c , vessels can be defined as the ratio of the pressure perturbation transmitted to the other two vessels to the pressure perturbation in the vessel where the initial wave is propagated. In Appendix 3 we show that $T^j = 1 + R_f^j$, $j = a, b, c$. These are effectively Kirchoff's laws at the junctions.

In normal conditions, the junctions in the aorta and first generation of bifurcations are close to well-matched for the propagation of waves travelling from the heart to the periphery; *i.e.* $R_f^a \approx 0$ [113, 114, 86]. Note that if $R_f^a = 0$ then $Y_0^a = Y_0^b + Y_0^c$ and, hence, $-1 < R_f^b = -Y_0^c/(Y_0^b + Y_0^c) < 0$ and $-1 < R_f^c = -Y_0^b/(Y_0^b + Y_0^c) < 0$. This means that the same junctions are necessarily poorly-matched for waves travelling from the periphery to the heart and generate reflected waves with a negative reflection coefficient. Thus, as waves travel progressively further down the generations of bifurcations of the arterial tree, their reflections effectively become trapped, with an ever diminishing proportion of their amplitude making the way back to proximal arteries. This *wave trapping* mechanism prevents distal changes in pressure and velocity from being seen in the proximal aorta [115].

Table 2 shows R_f^a , R_f^b and R_f^c in all the junctions of the 55-artery *normal young* model (M1), which are calculated using Eq. (19) with time-averaged radii and wave speeds.

The reflection coefficient at the outlet of each 1-D model terminal branch coupled to a single

resistance R_1 is [116]

$$R_f = \frac{R_1 - Z_0}{R_1 + Z_0}. \quad (20)$$

Note that $R_1 = Z_0$ yields $R_f = 0$; *i.e.* any incoming wave is completely absorbed by the 0-D model. For the RCR model in Fig. 13 (right), $R_1 = 0$ yields spurious wave reflections and $R_1 = Z_0$ minimises wave reflections [116]. We use the latter in all terminal branches of the different models.

At the aortic valve we can define a time-varying reflection coefficient, R_v , as the ratio of the pressure or flow change associated with the reflected pulse wave to that of the incident wave. We have $R_v > 1$ when the aortic valve is open and $R_v = 1$ when it is closed [117].

All these reflection coefficients can be expressed in terms of the characteristic flow variables w_f and w_b . We have $R_f^j = -w_f^j/w_b^j$ at the inlet ($R_v = -w_f/w_b$ at the aortic valve) and $R_t^j = w_f^j/w_b^j$ at the outlet of a segment Ω^j , $j = 1, \dots, N$.

Reflected waves are also generated due to pathologies in the arterial vasculature, such as stenosis [118] and aneurysms [108, 119].²⁸

3.3 Waveforms in the arterial network

Consider the arterial tree to be a network of N elastic and uniform arterial segments (or edges) Ω^i , $i = 1, \dots, N$, in which pulse wave propagation is modelled using the 0-D Eq. (18); initially without assuming periodicity. For convenience, we assume that $i = 1$ refers to the ascending aorta and $i = 2, \dots, M$ ($M < N$) refer to terminal segments. We also assume that the flow $q^1(0, t)$ is given and equal to the flow waveform at the inlet of the ascending aorta, $Q_{in}(t)$, and that the distal ends of Ω^j , $j = 2, \dots, M$, are coupled to matched RCR models (Fig. 13, right) relating q_{out}^j to $p_{e_{out}}^j$ through Eq. (14) with $Q = q_{out}^j$, $P_e = p_{e_{out}}^j$, and $R_1^j = Z_0^j$, $j = 2, \dots, M$.

Assuming $R_{0D}^i = 0$, $i = 1, \dots, N$, which is reasonable since fluid resistance in larger arteries is much smaller than peripheral resistances [2, Chap. 12]²⁹ we have the following important results.

Time-averaged solution

Under periodic flow conditions we have [101]

$$\overline{p^i} = P_{out} + R_T \overline{Q_{in}}, \quad i = 1, \dots, N, \quad \frac{1}{R_T} = \sum_{j=2}^M \frac{1}{R_2^j + Z_0^j}; \quad (21)$$

i.e. the cardiac output, $\overline{Q_{in}}$, outflow pressure, P_{out} , and net peripheral resistance, R_T , dictate the time-averaged (mean) pressure, $\overline{p^i}$, in any arterial segment Ω^i ($i = 1, \dots, N$) required to perfuse the microcirculation. Thus, mean pressures throughout the 1-D model arterial segments of the *normal* models (M1 and M2) are similar and smaller than in the *hypertensive* models (M3 and M4), which have a greater R_T (see Fig. 10a and Tables 3 and 4). Mean pressures are not exactly the same in the models with the same R_T due to the differences introduced by fluid viscous dissipation (through f) within the 1-D model segments. Changes in R_T have a small effect on pulse pressure (Fig. 10a), flow (Fig. 10b) and velocity (Fig. 11b) waveforms.

Inertia-free solution – The Windkessel effect

In general, for a non-periodic flow, the elastic component of blood pressure, $p_e(x, t)$, at any point in the arterial network tends to a space-independent Windkessel pressure, $p_w(t)$, with increasing

²⁸The expansions in cross-sectional area in these regions lead to flow recirculation, as can be shown using the conservation of momentum in Eq. (1) [63, p. 407]. Solving for $\frac{\partial P}{\partial x}$ and assuming a rigid wall expansion $A(x)$, inviscid fluid, a velocity profile with $\alpha = 1$, and an inflow to the expansion $Q(t)$ yields $\frac{\partial P}{\partial x} = -\frac{\rho}{A} \frac{dQ}{dt} + \frac{\rho Q^2}{A^3} \frac{dA}{dt}$. If the flow is decelerating and the area is diverging, positive pressure gradients can exist, which make flow separation and recirculation possible.

²⁹According to Poiseuille flow, flow resistance is inversely proportional to the fourth power of the vessel radius.

time t in diastole (Fig. 2, top). This is in agreement with *in vivo* data in the human and dog [120, 121] being approximately uniform during the last two thirds of diastole. We have [101]

$$p_w = P_{\text{out}} + (p_w(T_0) - P_{\text{out}})e^{-\frac{t-T_0}{R_T C_T}} + \frac{e^{-\frac{t}{R_T C_T}}}{C_T} \int_{T_0}^t \left(Q_{\text{in}}(t') + \sum_{j=2}^M \frac{C^j Z_0^j R_2^j}{R_2^j + Z_0^j} \frac{dq_{\text{out}}^j(t')}{dt'} \right) e^{\frac{t'}{R_T C_T}} dt', \quad t \geq T_0, \quad (22)$$

$$C_c = \sum_{i=1}^N C_{0D}^i, \quad C_p = \sum_{j=2}^M \frac{R_2^j C^j}{R_2^j + Z_0^j}, \quad (23)$$

where C_c is the total arterial conduit compliance, C_p is the total arterial peripheral compliance, $C_T = C_c + C_p$ is the total arterial compliance, and $p_w(T_0)$ is the pressure p_w at $t = T_0$. The total pressure $p^i(x, t)$ tends to $p_w + \gamma^i \left(\frac{\partial q}{\partial x} \right)^i$ ($i = 1, \dots, N$), in which γ^i and $\left(\frac{\partial q}{\partial x} \right)^i$ may be different for each arterial segment. Fig. 9 (right) shows the analog electric circuit satisfied by p_w .

Equation (22) is obtained by setting $L_{0D}^i = 0$, $i = 1, \dots, N$. Therefore, fluid inertia becomes negligible compared to wall compliance and fluid peripheral resistance with the increasing time in diastole, so that changes in pressure can be assumed to occur synchronously throughout the arteries. Global properties govern these changes: the total arterial compliance, C_T , net peripheral resistance, R_T , outflow pressure, P_{out} , and flow at the inlet of the ascending aorta, Q_{in} ³⁰. Wall visco-elasticity accounts for the differences in total pressure among the different arterial segments.

Although p_w fails to reproduce the wave-like nature of pulse propagation during systole and early diastole, it provides a 0-D order approximation to the nonlinear pressure $P(x, t)$ in larger systemic arteries, which allows us to study the (global) effects of C_T , R_T , P_{out} and Q_{in} . According to Eq. (22), C_T and R_T smooth the intermittent flow out of the heart, Q_{in} (Fig. 2, bottom left), through the term $e^{\frac{t'}{R_T C_T}}$ in the integral. The term $1/C_T$ multiplying the integral affects the peak p_w produced by Q_{in} in systole. Thus, the pulse pressure of p_w (and hence $P(x, t)$) in *young* models (M1 and M3) is smaller than in *old* models (M2 and M4) (Fig. 10a,c), since the former have more compliant arteries (*i.e.* greater C_T) than the latter (Table 3). These mechanisms are usually referred to as the *Windkessel effect*³¹.

The aorta and other larger arteries behave as a compliance chamber. They provide a reservoir of high pressure that drives blood flow during diastole, producing smooth and non-intermittent pressure and flow waveforms throughout the vasculature (Fig. 2). By the time blood reaches the capillary beds, its flow is relatively steady and slow, which facilitates diffusive exchange of nutrients and waste products between the blood and the surrounding tissue.

In vivo measurements in humans show an increase in pulse pressure³² with age [91] and disease (such as atherosclerosis and diabetes) [126], which may be explained through the role played by C_T in the Windkessel effect. Ageing increases the stiffness³³ of the arterial wall and, hence, decreases C_T . A smaller C_T also reduces the ability of the Windkessel effect to smooth the cardiac output [95]. Indeed the amplitude of the Windkessel flow $q_w = (p_w - P_{\text{out}})/R_T$ is greater in *old* models (M2 and M4) than in *young* models (M1 and M3) (Fig. 10d).

If arteries were very rigid (*i.e.* C_T were very small) then pulse wave speeds, c_0 , would be very large (Eq. (17))³⁴ and, hence, pressure changes would occur almost synchronously throughout the cardiac cycle. Thus, pressures elsewhere in the system would be very similar to the intermittent

³⁰Despite $Q_{\text{in}} \approx 0$ during normal diastolic conditions, $p_w(T_0)$ depends on the systolic part of $Q_{\text{in}}(t)$.

³¹The smoothing or buffering effect of the elastic arteries was noted in the 17th century by Borelli and in the 18th century by Hales, who compared it to the effect of the ‘air chamber’ in fire engine pumps. In 1899 Frank made the concept quantitative and called it the *Windkessel effect* using the German translation of ‘air chamber’ [17].

³²Pulse pressure has been found to be an important predictor of cardiovascular events that cause morbidity and mortality [122, 123, 124, 125, 126]. It is also increasingly been recognised an important factor in the pathogenesis of atherosclerosis [126].

³³Premature stiffening may occur with disease. Note that arterial stiffness, unlike arterial compliance and distensibility, is a purely descriptive term that cannot be measured or quantified.

³⁴Fig. 10a,b shows an earlier arrival of the foot of the pulse wave in models with a smaller C_T (M2 and M4).

pressures of the left ventricle. Under these circumstances, the ventricle would need to contract more vigorously³⁵ to expel the same volume of blood and quicker to provide a steady blood supply to the microcirculation. Therefore, it would be more likely to develop *hypertrophy* (a heart muscle disease) and to fail [127].

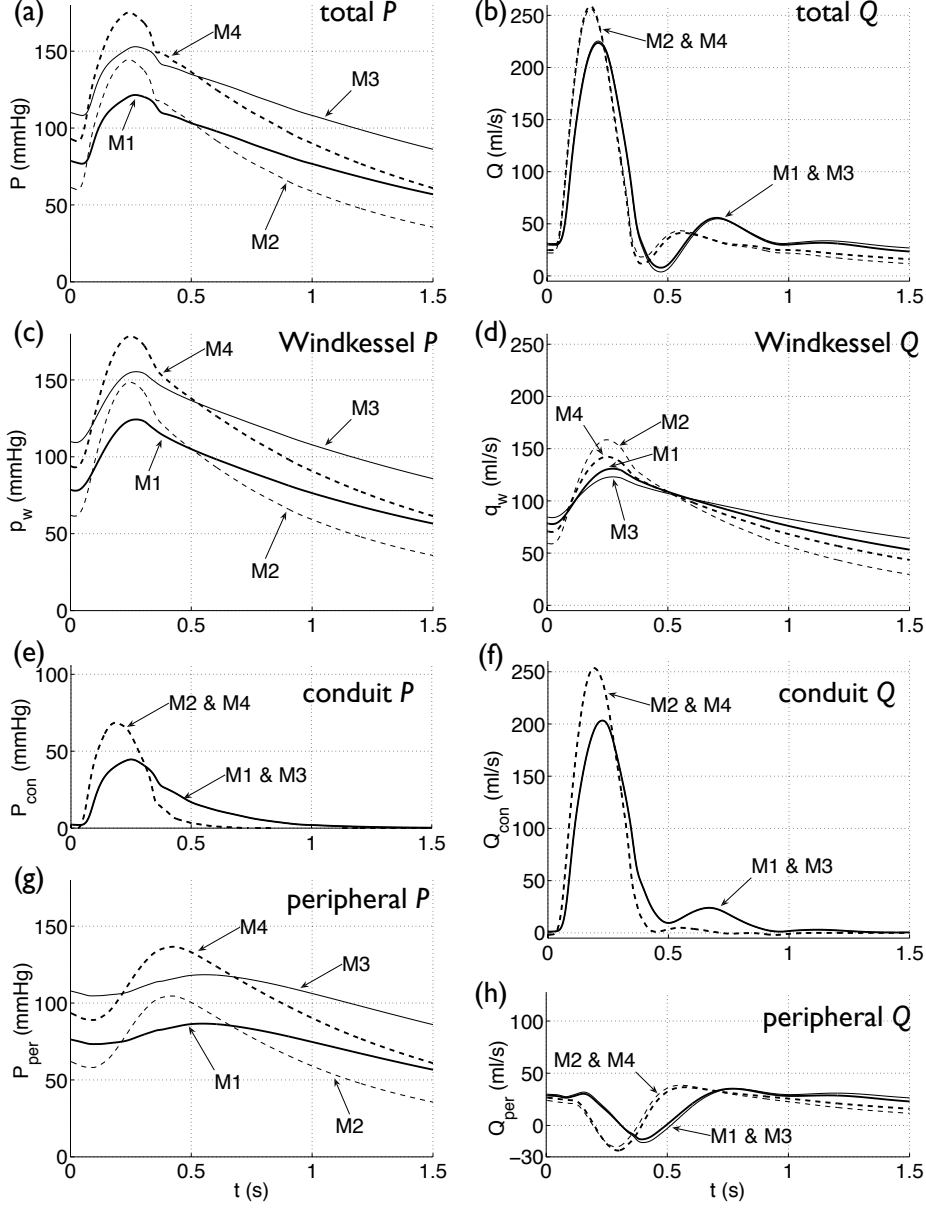


Figure 10: Total (a,b), Windkessel (c,d), conduit (e,f) and peripheral (g,h) pressures (left) and flow rates (right) with time in the thoracic aorta (Segment 27) of the different models (Fig. 2, centre). Note that the flow rate at the aortic root was set to zero ($Q_{\text{in}} = 0$) at the start of the second quasi-steady cardiac cycle (*i.e.* cardiac contraction was stopped to simulate an *asystole*), to prolong pressure and flow decays.

The effect of R_T on p_w is the same as that described for blood pressure using Eq. (21). During diastole the aortic valve is closed and, hence, $Q_{\text{in}} = 0$, which reduces Eq. (22) to an approximately exponential decay to the asymptote P_{out} with a time constant $R_T C_T$. If $C^j = 0$, $j = 2, \dots, M$, then p_w is exactly the Windkessel pressure introduced by Frank [110], which becomes a mono-exponential curve with time constant $R_T C_T$ during diastole.³⁶

³⁵We have recently shown that $p_w(t)$ minimises the ventricular hydraulic work for any physiologically or clinically reasonable Q_{in} , C_T and R_T [31].

³⁶Note that the linearised system also features a local time constant $Z_0^i C_{0D}^i = l^i / c_0^i$ for each arterial segment Ω^i , $i = 1, \dots, N$, which is equal to the time it takes a wave to travel the length l^i of Ω^i .

3.4 Peripheral and conduit waveforms

Neglecting nonlinear effects, we can post-process the 1-D model results and separate the pressure and flow waveforms at an arbitrary point in the arterial network into a component made up of all pulse waves that originated at the periphery, which we call the *peripheral waveform*, and a component made up of the rest of pulse waves (these are the result of reflections at the internal junctions and aortic root), which we call it the *conduit waveform*.

As detailed in [128], the conduit waveform is obtained by running the original simulation with terminal branches coupled to single resistances that completely absorb any incident wave; *i.e.* $R_1^j = Z_0^j$, $j = 1, \dots, M$ (see Eq. (20)). The peripheral waveform is the difference between the total waveform and the conduit waveform.

The pressure fall off in diastole is mainly generated by the peripheral waveform (Figs. 10e,g, 12a,c), whereas the shape of the pressure waveform earlier in the cardiac cycle (including the diastolic notch) strongly depends on the conduit waveform. Most of the thoracic flow signal is generated by the conduit waveform (Fig. 10f) with the peripheral waveform featuring some reversed flow (Fig. 10h). It is also important to note that most of the conduit waveform vanishes at the end of the cardiac cycle, whereas the peripheral waveform does not. This suggests a strong influence of peripheral reflections originating in previous cardiac cycles.

Decreasing the total compliance, C_T , increases the amplitude of both the conduit and peripheral waveforms (Fig. 10e,g). Changes in the net resistance R_T , however, only affect the peripheral waveforms (Fig. 10e,g). These results suggest that arterial stiffness (which dictates C_T) has a similar effect on reflections originated at internal junctions and aortic root to those originated at the periphery, whereas peripheral resistances only affect reflections originated at the periphery. That is, ‘conduit’ and ‘peripheral’ mechanisms underlie changes in pulse pressure, whereas only ‘peripheral’ mechanisms underlie changes in mean pressure.

4 Pulse wave analysis using *in vivo* data

The results shown in Section 3 rely on an accurate knowledge of all the physical properties of the system. In *in vivo* studies, however, we have far less data available; in many cases only a few measurements of pressure, flow and arterial wall displacement. Blood velocity and flow (including the cardiac output) can be measured with time using Doppler ultrasound [89] and magnetic resonance (MR) [88, 47, 83]. In animal studies, invasive flow measurements can be obtained using electromagnetic flowmeters, fluorescent microspheres, scintigraphy and laser Doppler anemometry. Blood pressure can be recorded noninvasively in superficial arteries, such as carotid, brachial, radial and femoral, using applanation tonometry [53, 62, 129, 47, 83]. Invasive measurements of pressure and velocity can be obtained in the aorta and other extracranial arteries using pressure- and flow-sensing catheters [130]. The internal luminal area can be measured in superficial arteries using ultrasound-based echo-tracking [53, 62, 131] and MR [88]. Invasive measurements using piezoelectric crystal transducers have been carried out in animal experiments [62].

Several methods have been developed for the analysis of *in vivo* data in both the time and frequency domains [16, 132]. Here we briefly describe tools that allow us to separate the pulse waveform into physically relevant components (Section 4.1), calculate the aortic pressure from a non-invasive peripheral measurement (Section 4.2), study the energy carried by the pulse wave (Section 4.3) and estimate clinically relevant parameters (Section 4.4). We also mention some examples of clinically relevant applications of 1-D modelling (Section 4.5).

4.1 Wave separations

Changes in the forward and backward characteristic variables, $W_{f,b}$, at an arbitrary point in the network (Fig. 4) can be written in terms of the corresponding changes in pressure, $P_{f,b}$, and

velocity, $U_{f,b}$, if the local pulse wave speed c is known [100, 133].³⁷ This separation provides valuable information on the conditions of the system upstream and downstream of the measurement site in normal and pathological conditions [135].

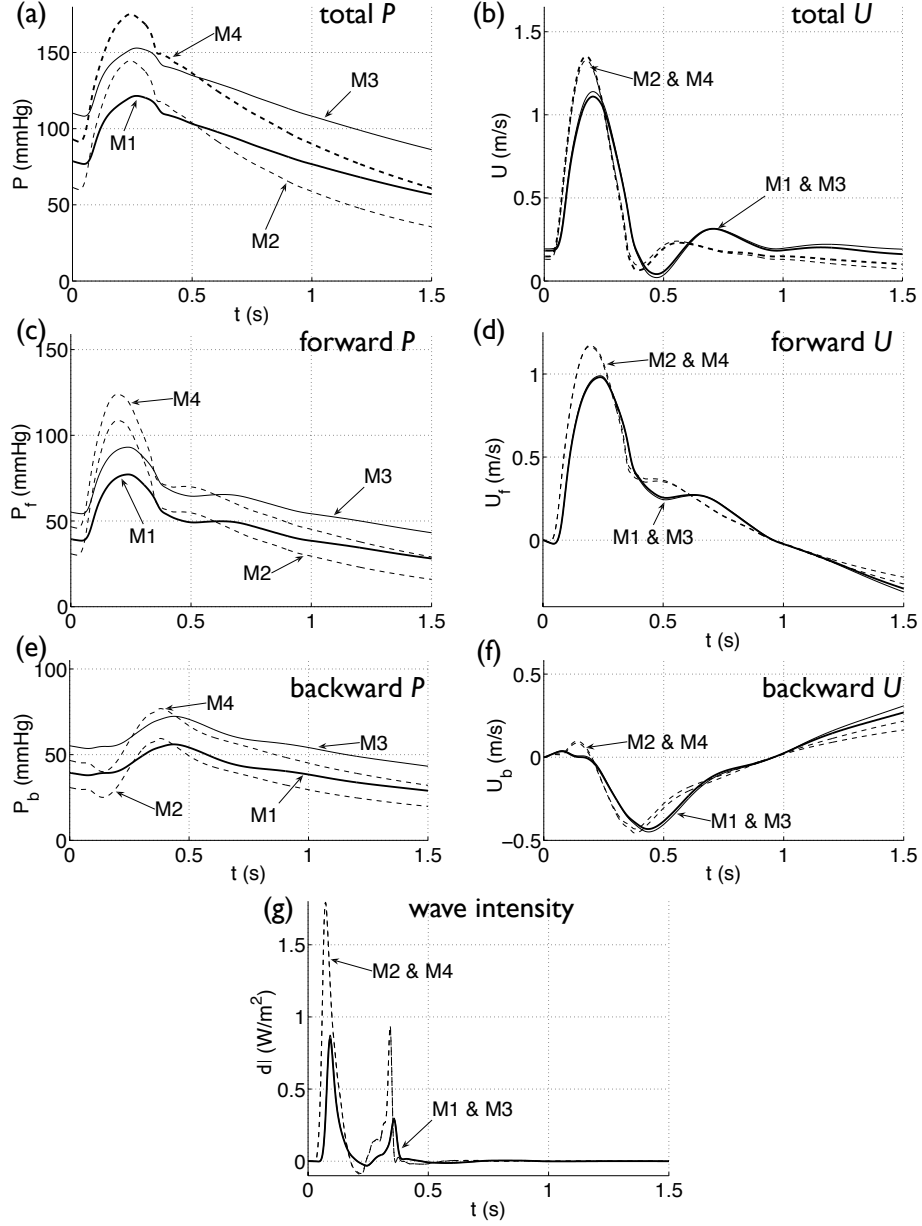


Figure 11: Pressure (a) and velocity (b) with time in the thoracic aorta (Segment 27) of the different models (Fig. 2, centre). From these data we can calculate the following waveforms (as described in the text): the forward and backward components of pressure and velocity (c)–(f), and the wave intensity waveform (g). An integration constant was included arbitrarily in the forward and backward pressure and was taken to be the minimum value of pressure. The integration constant for velocity was zero. Note that the flow rate at the aortic root was set to zero ($Q_{in} = 0$) at the start of the second quasi-steady cardiac cycle to prolong pressure and flow decays.

The increase in P_f in early systole while P_b is still decaying (Fig. 12b,d) indicates that the changes in pressure produced by cardiac contraction initially propagate away from the heart. The increase in P_b later in systole indicates the arrival of reflected waves, generated at points of impedance mismatch as described in Section 3.2. In diastole P_f and P_b are similar, suggesting that

³⁷This separation can also be achieved in the frequency domain when nonlinear terms are neglected [134].

P is made up of approximately equal amounts of upstream and downstream wave reflections³⁸.

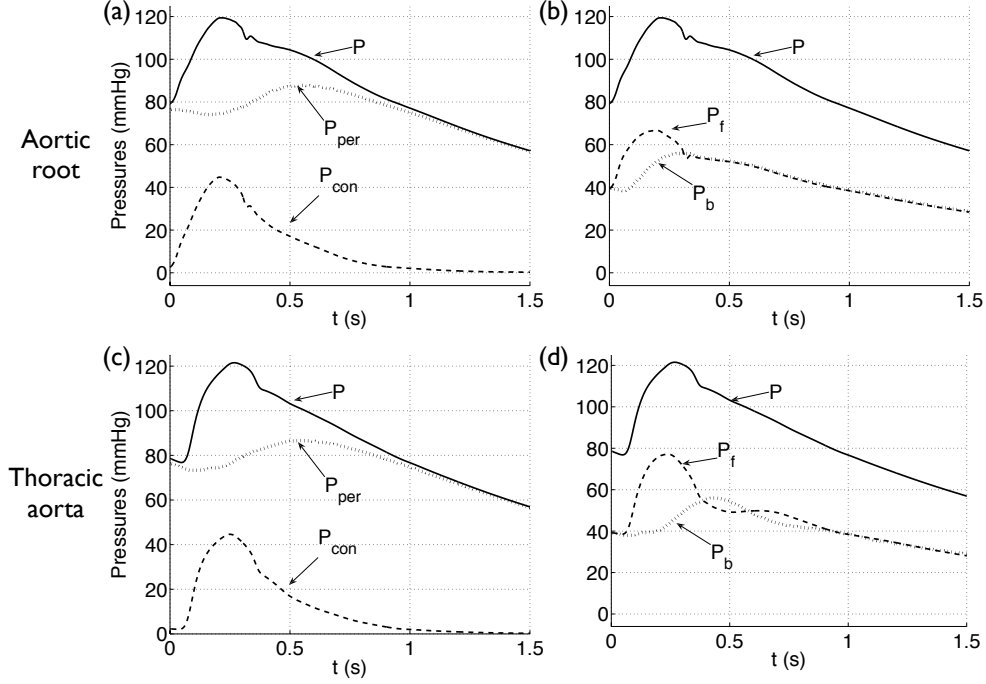


Figure 12: Pressure with time in the aortic root (Segment 1) (top) and thoracic aorta (Segment 27) (bottom) of the *normal young* model (M1) (Fig. 2, centre). They are separated into conduit and peripheral pressures (a,c) and forward and backward pressures (b,d). Note that the flow rate at the aortic root was set to zero ($Q_{in} = 0$) at the start of the second quasi-steady cardiac cycle to prolong pressure and flow decays.

Changes in C_T and R_T have a similar effect as previously discussed for the total pressure. The amplitudes of P_f and P_b are similar in models with similar C_T (*young* and *old*, Fig. 11c,e) and increase with the decreasing C_T by approximately the same percentage (about two-fold when comparing P_f and P_b in *young* models with the corresponding waveforms in *old* models). Changes in R_T affect the magnitude of P_f and P_b , but not their shape.

Note that P_f and U_f have the same shape, but U_b is inverted with respect to P_b . Thus, peripheral reflections yield negative U_b that decrease the magnitude of the velocity waveform at the thoracic aorta in late systole and early diastole (Fig. 11f). Changes in C_T and R_T affect U_f and U_b less than they do P_f and P_b (Fig. 11d,f).

Other separations of the pressure waveform have been proposed, *e.g.* the *reservoir-wave hypothesis* to quantify the buffering function of the larger conduit arteries from *in vivo* measurements of pressure and flow [120, 136, 121, 128]. It separates the pressure waveform into a space-independent *reservoir* component that is based on the Windkessel pressure, p_w (and hence depends on global parameters), and an *excess* component that changes in time and space according to local properties (geometry and local compliance). This separation is proving very useful to understand the outcome of large studies on hypertensive drugs [137].

4.2 Transfer functions

The ascending aortic (or *central*) pressure seems to be a better predictor of cardiovascular events than more peripheral pressures (*e.g.* radial and brachial pressures) [138, 139, 126]; perhaps because it is closer to the heart. Direct measurement of the aortic pressure, unlike the peripheral pressure, can only be obtained invasively. However, there are transfer functions that calculate aortic pressure from peripheral pressure using Fourier analysis [140, 141, 142]. According to [142], an accurate

³⁸Many of these reflected waves were generated in previous cardiac cycles.

individualised description of pressure transfer can be obtained with a non-invasively measured travel time from the ascending aorta to the peripheral site.

4.3 Wave intensity analysis

In wave intensity analysis the pulse waveform is decomposed into successive pressure and velocity wavefronts³⁹ to study the flux of energy per unit area (which is called *wave intensity*⁴⁰) carried by the pulse wave, $dI = dP dU$, where dP and dU are the changes in pressure and velocity across a wavefront, respectively. The quantity dI can be calculated from simultaneous pressure and flow measurements at an arbitrary location in the arterial network. It is positive for forward-travelling wavefronts and negative for backward wavefronts. Therefore, the net wave intensity reveals whether forward or backward wavefronts are dominant and how big they are at any particular time during the cardiac cycle. Thus, wave intensity allows us to quantify the timing, direction and magnitude of dominant wavefronts (both compression and expansion) over the cardiac cycle [143, 100].

Wave intensity analysis assumes neither periodicity nor linearity and is based on the one-dimensional formulation of arterial blood flow described in Section 2. This analysis provides valuable information to understand the role of wave reflections on blood flow in systemic arteries [144, 145, 146, 147, 148, 129], including the coronary circulation [149, 69].

The contour of dI in Fig. 11g, which is generated from the simulated data in the thoracic aorta of the different models, has the typical shape observed *in vivo* in the aorta under normal conditions [143]. The first peak of dI corresponds to the initial compression (or acceleration) wavefront caused by the contraction of the left ventricle. In mid-systole there is a small negative peak indicating a dominant reflection of the initial contraction wavefront. This is followed by a second positive peak indicating a dominant forward wavefront at the end of systole, which represents a decompression (or deceleration) wave generated by the relaxation of the left ventricle.

The positive and negative peaks of dI increase with decreasing C_T ; *i.e.* the energy carried by the pulse wave in *old* models (M2 and M4) is greater than in *young* models (M1 and M3) (Fig. 11g), suggesting that the left ventricle must contract more vigorously to propel the same amount of blood flow throughout the vasculature. On the other hand, changes in R_T do not significantly affect the contour of dI , suggesting a minor effect of peripheral reflections on the flux of energy in the thoracic aorta. *In vivo* studies at the ascending aorta have shown that the magnitude and arrival time of the backward compression wave in mid-systole varies with age, diseases, arterial compliance and vascular tone [146, 150].

4.4 Parameter estimations

The 1-D formulation allows us to use haemodynamic data that can be measured *in vivo* to calculate properties of the cardiovascular system that cannot be directly measured *in vivo*. Several optimisation algorithms have been proposed; *e.g.* Kalman filtering techniques for the peripheral boundary conditions [59], an adjoint state approach for the local compliance [151], and local sensitivity indices for several mechanical properties of the arteries of the arm [152]. Estimation algorithms have also been proposed to calculate parameter values based upon a mechanical understanding of the effect that the parameter has on haemodynamic quantities that can be measured clinically. This is the approach followed in [153, 130], for example, to calculate the local pulse wave speed from simultaneous pressure and velocity measurements, and in [116, 47] to distribute the net peripheral resistance and compliance among the terminal branches of 1-D models. Several lumped parameter models have been used to estimate global properties of the arterial tree by fitting the model to measured pressure and flow data [154, 155].

The accuracy of estimation algorithms can be tested using 1-D model waveforms, which are free of measurement and alignment errors⁴¹. Numerically we can compare the estimates with the

³⁹Mathematically, a wavefront refers to an infinitesimal change in pressure, dP , and velocity, dU .

⁴⁰Wave intensity is a term analogous to acoustic intensity.

⁴¹Interferences and differences in the temporal resolution or bandwidth between the measurement equipment can

theoretical values calculated from the parameters of the 1-D model [101, 158, 159, 160, 161, 152]. This is particularly relevant when the estimation algorithms are based on the 1-D formulation. The sensitivity of the 1-D model to several parameters is studied in [74, Ch. 4], [82, 161, 142].

4.5 Clinically relevant applications of 1-D modelling

Although 1-D modelling is still a research tool, several studies have explored its clinical potential. In addition to assess the accuracy of estimation algorithms (see Section 4.4), 1-D modelling has been applied to (i) study the effects of stenoses on pulse wave propagation [106, 82, 97, 162], (ii) assess indices and procedures used in clinical practice that are based on pulse wave analysis, such as the aortic augmentation index in systolic hypertension studies [163, 164], (iii) the study and identification of anatomical variations in the cerebral [165, 166, 72, 77] and arm [73] arterial networks, (iv) the noninvasive assessment of vascular function [86], and (v) investigate the outcome of surgical procedures, such as arterial bypass grafting [167, 67, 168, 169, 74] and arterio-venous fistulae for vascular access in dialysis patients [170, 171].

5 Concluding remarks and challenges ahead

We have shown the usefulness of results on arterial wave mechanics in the systemic circulation that are based on the 1-D formulation. Haemodynamics in this part of the cardiovascular system has been widely researched, since it is exposed to many life-threatening conditions and diseases, such as hypertension and atherosclerosis, which are influenced by haemodynamic conditions.

The 1-D formulation is particularly suited to study large-scale mechanisms underlying the pulse waveform in the arterial system as a whole. The very large scales of pulse wavelengths compared to arterial lengths and diameters allow us to relax the modelling assumptions and reduce the number of parameters that would be required to simulate the full 3-D problem. With less parameters to be determined, it is relatively easier to obtain patient-specific models. For example, we have seen that the *global* parameters that define the windkessel pressure, $p_w(t)$ (see Eq. (22)), play a key role in defining the pressure waveform in larger arteries. These parameters (cardiac ejection, total compliance, net peripheral resistance, and outflow pressure) can be estimated from a few *in vivo* measurements of pressure and flow rate [101, 155].

The 1-D formulation allows us to study clinically relevant haemodynamic mechanisms that are often first observed through correlations, suggest and test new tools for the estimation of important parameters of the cardiovascular system (*e.g.* arterial compliance and distensibility [160, 158, 159]) and assess indices and procedures used in clinical practice that are based on pulse wave analysis. The methods developed to study 1-D arterial wave mechanics can be applied directly to the study of venous wave mechanics, taking into account the anatomical and physiological differences that exist between arteries and veins [1, 2, 36, 37, 172].

A 1-D approach, however, does not allow us to compute detailed flow patterns at each point in the arterial tree, for which computationally far more expensive 3-D models, which account for the three spatial dimensions of the problem, are necessary; *e.g.* to calculate WSS (see [173] for an early example and [174, 175, 87, 176] for more recent studies). Nevertheless, the 1-D formulation can provide improved boundary conditions for 3-D models of localised areas of the vasculature; in the so-called *3-D/1-D multi-scale coupling* [30, 177, 178, 179, 180, 181, 182].

In our opinion, the challenges ahead for 1-D modelling are to develop tools to accurately estimate model parameters (such as wall distensibility and peripheral boundary conditions) and to verify the 1-D formulation and parameter estimation tools using *in vivo* data, ideally in the human. Further tests should also be carried out by comparison against numerical data generated using 3-D pulsatile models in deformable domains. These tests, should provide a clearer picture of the advantages and limitations of using 1-D modelling as a clinical tool. Application of 1-D modelling to

introduce phase delays that may be significant and large enough to spoil the acquisition of simultaneous measurements at the same location [156, 157].

study the physical mechanisms underlying variations in the pulse waveform due to postural changes and clinical manoeuvres requires accurate models of neurogenic and hormonal control mechanisms. There are lumped parameter control models that are governed by ordinary differential equations and which could be coupled to a 1-D model of the larger arteries (*e.g.* [183]).

We believe that modelling and analysis (*e.g.* wave intensity analysis) based on the 1-D formulation are powerful tools to interpret *in vivo* data, making the most of the usually limited amount of data available in the clinic to improve the understanding, diagnosis and treatment of disease.

Acknowledgements

Jordi Alastruey gratefully acknowledges the support of a British Heart Foundation Intermediate Basic Science Research Fellowship (FS/09/030/27812) and the Centre of Excellence in Medical Engineering funded by the Wellcome Trust and EPSRC under grant number WT 088641/Z/09/Z.

References

- [1] J.R. Levick. *An Introduction to Cardiovascular Physiology*. Hodder Arnold, UK, London, 5th edition, 2010.
- [2] C.G. Caro, T.J. Pedley, R.C. Schroter, and W.A. Seed. *The Mechanics of the Circulation*. Cambridge University Press, 2nd edition, 2011.
- [3] P. Scarborough, P. Bhatnagar, K. Wickramasinghe, K. Smolina, C. Mitchell, and M. Rayner. Coronary heart disease statistics. British Heart Foundation Statistics Database (www.heartstats.org), 2010.
- [4] S. Allender, P. Scarborough, V. Peto, M. Rayner, J. Leal, R. Luengo-Fernandez, and A. Gray. European cardiovascular disease statistics. British Heart Foundation Statistics Database (www.heartstats.org), 2008.
- [5] M. Ezzati, A.D. Lopez, A. Rodgers, H.S. Vanders, and C.J. Murray. Selected major risk factors and global and regional burden of disease. *Lancet*, 360:1347–1360, 2002.
- [6] C.G. Caro, J.M. Fitzgerald, and R.C. Schroter. Atheroma and arterial wall shear. Observation, correlation and proposal of a shear dependent mass transfer mechanism for atherogenesis. *Proc. R. Soc. Lond. B*, 177:109–133, 1971.
- [7] A.M. Malek, S.L. Alper, and S. Izumo. Hemodynamic shear stress and its role in atherosclerosis. *JAMA*, 282:2035–2042, 1999.
- [8] S. Laurent, P. Boutouyrie, R. Asmar, I. Gautier, B. Laloux, L. Guize, P. Ducimetiere, and A. Benetos. Aortic stiffness is an independent predictor of all-cause and cardiovascular mortality in hypertensive patients. *Hypertension*, 37:1236–1241, 2001.
- [9] C. Vlachopoulos, K. Aznaouridis, and C. Stefanadis. Prediction of cardiovascular events and all-cause mortality with arterial stiffness: a systematic review and meta-analysis. *J. Am. Coll. Cardiol.*, 55:1318–1327, 2010.
- [10] S. Glagov, C. Zarins, D.P. Giddens, and D.N. Ku. Hemodynamics and atherosclerosis: insights and perspectives gained from studies of human arteries. *Arch. Pathol. Lab. Med.*, 112:1018–1031, 1988.
- [11] J. Gariepy, M. Massonneau, J. Levenson, D. Heudes, and A. Simon. Evidence for in vivo carotid and femoral wall thickening in human hypertension. Groupe de Prévention Cardio-vasculaire en Médecine du Travail. *Hypertension*, 22:111–118, 1993.
- [12] L. Euler. Principia pro motu sanguinis per arterias determinando. *Opera posthuma mathematica et physica anno 1844 detecta*, 2:814–823, 1775. Ediderunt P.H. Fuss et N. Fuss Petropoli; Apud Eggers et Socios.
- [13] J.W.S. Rayleigh. *The Theory of Sound, Volume One*. Macmillan, 1894.
- [14] T.J.R. Hughes. *A study of the one-dimensional theory of arterial pulse propagation*. PhD thesis, Report 74-13, University of California Berkeley, Structural Engineering Laboratory, 1974.
- [15] T.J. Pedley. *The Fluid Mechanics of Large Blood Vessels*. Cambridge University Press, 1980.
- [16] W.W. Nichols and M.F. O’Rourke. *McDonald’s Blood Flow in Arteries: Theoretical, Experimental and Clinical Principles*. Edward Arnold, London, 5th edition, 2005.
- [17] K.H. Parker. A brief history of arterial wave mechanics. *Med. & Biol. Eng. & Comput.*, 47:111–118, 2009.
- [18] T.J.R. Hughes and J. Lubliner. On the one-dimensional theory of blood flow in the larger vessels. *Math. Biosciences*, 18:161–170, 1973.
- [19] S.J. Sherwin, V.E. Franke, J. Peiró, and K.H. Parker. One-dimensional modelling of a vascular network in space-time variables. *J. Eng. Maths.*, 47:217–250, 2003.
- [20] F.N. van de Vosse and N. Stergiopulos. Pulse wave propagation in the arterial tree. *Annu. Rev. Fluid Mech.*, 43:467–499, 2011.

- [21] N. Westerhof, J.-W. Lankhaar, and B.E. Westerhof. The arterial Windkessel. *Med. & Biol. Eng. & Comput.*, 47:131–141, 2009.
- [22] M. Zamir. *The physics of pulsatile flow*. Biological and Medical Physics Series. Springer-Verlag (New York), 2000.
- [23] W.A. Seed and N.B. Woods. Velocity patterns in the aorta. *Cardiov. Res.*, 5:319–330, 1971.
- [24] P.D. Stein and H.N. Sabbah. Turbulent blood flow in the ascending aorta of humans with normal and diseased aortic valves. *Circulation Research*, 39:58–65, 1976.
- [25] N.P. Smith, A.J. Pullan, and P.J. Hunter. An anatomically based model of transient coronary blood flow in the heart. *SIAM J. Appl. Math.*, 62:990–1018, 2001.
- [26] B.W. Schaaf and P.H. Abbrecht. Digital computer simulation of human systemic arterial pulse wave transmission: a nonlinear model. *J. Biomech.*, 5:345–364, 1972.
- [27] J.C. Stettler, P. Niederer, and M. Anliker. Theoretical analysis of arterial hemodynamics including the influence of bifurcations. Part I: Mathematical model and prediction of normal pulse patterns. *Ann. Biomed. Eng.*, 9:145–164, 1981.
- [28] A.M. Robertson and H. Zakaria. One-dimensional non-Newtonian models for arterial flows. In *American Physical Society, 57th Annual Meeting of the Division of Fluid Dynamics, 21-23 November, 2004, Seattle, Washington*, 2004.
- [29] A.M. Robertson, A. Sequeira, and M.V. Kamenewa. Hemorheology. In G.P. Galdi, R. Rannacher, A.M. Robertson, and S. Turek, editors, *Hemodynamical Flows. Modeling, Analysis and Simulation. Oberwolfach Seminars*, volume 37, pages 63–120. Birkhäuser Verlag Basel, Switzerland, 2008.
- [30] L. Formaggia, J.F. Gerbeau, F. Nobile, and A. Quarteroni. On the coupling of 3D and 1D Navier-Stokes equations for flow problems in compliant vessels. *Comp. Meth. App. Mech. Eng.*, 191:561–582, 2001.
- [31] K.H. Parker, J. Alastruey, and G.-B. Stan. Arterial reservoir-excess pressure and ventricular work. *Med. & Biol. Eng. & Comput.*, 50:419–424, 2012.
- [32] C. Sheng, S.N. Sarwal, K.C. Watts, and A.E. Marble. Computational simulation of blood flow in human systemic circulation incorporating an external force field. *Med. & Biol. Eng. & Comput.*, 33:8–17, 1995.
- [33] J.B. Grotberg and O.E. Jensen. Biofluid mechanics in flexible tubes. *Annu. Rev. Fluid Mech.*, 36:121–147, 2004.
- [34] S.J. Payne. Analysis of the effects of gravity and wall thickness in a model of blood flow through axisymmetric vessels. *Med. & Biol. Eng. & Comput.*, 42:799–806, 2004.
- [35] M.S. Olufsen, J.T. Ottesen, H.T. Tran, L.M. Ellwein, L.A. Lipsitz, and V. Novak. Blood pressure and blood flow variation during postural change from sitting to standing: model development and validation. *J. Appl. Physiol.*, 99:1523–1537, 2005.
- [36] B.S. Brook and T.J. Pedley. A model for time-dependent flow in (giraffe jugular) veins: uniform tube properties. *J. Biomech.*, 35:95–107, 2002.
- [37] J.M. Fullana and S. Zaleski. A branched one-dimensional model of vessel networks. *J. Fluid Mech.*, 621(183–204), 2009.
- [38] J. Peiró and A. Veneziani. Reduced models of the cardiovascular system. In L. Formaggia, A. Quarteroni, and A. Veneziani, editors, *Cardiovascular Mathematics. Modeling and Simulation of the Circulatory System*, pages 347–394. Springer-Verlag (Milano), 2009.
- [39] S. Čanić and E.H. Kim. Mathematical analysis of the quasilinear effects in a hyperbolic model of blood flow through compliant axi-symmetric vessels. *Math. Meth. Appl. Sci.*, 26:1161–1186, 2003.
- [40] A. Quarteroni and L. Formaggia. *Mathematical modelling and numerical simulation of the cardiovascular system*. In: N. Ayache (ed.), *Modelling of Living Systems*. Elsevier (Amsterdam), 2004.
- [41] D.A. McDonalds. *Blood Flow in Arteries*. Edward Arnold, London, 1974.
- [42] M.S. Olufsen, C.S. Peskin, W.Y. Kim, E.M. Pedersen, A. Nadim, and J. Larsen. Numerical simulation and experimental validation of blood flow in arteries with structured-tree outflow conditions. *Annals Biomed. Eng.*, 28:1281–1299, 2000.
- [43] S. Čanić, D. Lamponi, A. Mikelić, and J. Tambača. Self-consistent effective equations modeling blood flow in medium-to-large compliant arteries. *Multiscale Mod. Sim.*, 3:559–596, 2005.
- [44] A.M. Robertson and A. Sequeira. A director theory approach for modeling blood flow in the arterial system: An alternative to classical 1D models. *Mathem. Mod. and Meth. App. Sci.*, 15:871–906, 2005.
- [45] K. Azer and C.S. Peskin. A one-dimensional model of blood flow in arteries with friction and convection based on the Womersley velocity profile. *Cardiov. Eng.*, 7:51–73, 2007.
- [46] D. Bessems, M. Rutten, and F. van de Vosse. A wave propagation model of blood flow in large vessels using an approximate velocity profile function. *J. Fluid Mech.*, 580:145–168, 2007.

- [47] P. Reymond, F. Merenda, F. Perren, D. Rüfenacht, and N. Stergiopoulos. Validation of a one-dimensional model of the systemic arterial tree. *Am. J. Physiol. Heart Circ. Physiol.*, 297:H208–H222, 2009.
- [48] Y.C. Fung. *Biomechanics: Mechanical properties of living tissues*. Springer-Verlag (New York), 2nd edition, 1993.
- [49] G.A. Holzapfel, T.C. Gasser, and R.W. Ogden. A new constitutive framework for arterial wall mechanics and a comparative study of material models. *J. Elasticity*, 61:1–48, 2000.
- [50] R.L. Armentano, J.G. Barra, F.M. Pessana, D.O. Craiem, S. Graf, D.B. Santana, and R.A. Sanchez. Smart smooth muscle spring-dampers. Smooth muscle smart filtering helps to more efficiently protect the arterial wall. *IEEE Eng. Med. Biol. Mag.*, 26:62–70, 2007.
- [51] C.V. Ioannou, N. Stergiopoulos, A.N. Katsamouris, I. Startchik, A. Kalangos, M.J. Licker, N. Westerhof, and D.R. Morel. Hemodynamics induced after acute reduction of proximal thoracic aorta compliance. *Eur. J. Vasc. Endovasc. Surg.*, 26:195–204, 2003.
- [52] R. Armentano, J. Barra, J. Levenson, A. Simon, and R.H. Pichel. Arterial wall mechanics in conscious dogs: Assessment of viscous, inertial, and elastic moduli to characterize aortic wall behavior. *Circulation Research*, 76:468–478, 1995.
- [53] R. Armentano, J.L. Megnien, A. Simon, F. Bellenfant, J. Barra, and J. Levenson. Effects of hypertension on viscoelasticity of carotid and femoral arteries in humans. *Hypertension*, 26:48–54, 1995.
- [54] D. Craiem, S. Graf, F. Pessana, J. Grignola, D. Bia, F. Gines, and R. Armentano. Cardiovascular engineering: modelization of ventricular arterial interaction in systemic and pulmonary circulation. *Latin American Applied Research*, 35:111–114, 2005.
- [55] S. Čanić, J. Tambača, G. Guidoboni, A. Mikelić, C. Hartley, and D. Rosenstrauch. Modeling viscoelastic behavior of arterial walls and their interaction with pulsatile blood flow. *SIAM J. Appl. Math.*, 67:164–193, 2006.
- [56] M. Saito, Y. Ikenaga, M. Matsukawa, Y. Watanabe, T. Asada, and P.-Y. Lagrée. One-dimensional model for propagation of a pressure wave in a model of the human arterial network: Comparison of theoretical and experimental results. *J. Biomech. Eng.*, 133:121005, 2011.
- [57] J. Alastruey, A.W. Khir, K.S. Matthys, P. Segers, S.J. Sherwin, P. Verdonck, K.H. Parker, and J. Peiró. Pulse wave propagation in a model human arterial network: Assessment of 1-D visco-elastic simulations against *in vitro* measurements. *J. Biomech.*, 44:2250–2258, 2011.
- [58] L. Formaggia, D. Lamponi, and A. Quarteroni. One-dimensional models for blood flow in arteries. *J. Eng. Math.*, 47:251–276, 2003.
- [59] K. Devault, P. Gremaud, V. Novak, M. Olufsen, G. Vernières, and P. Zhao. Blood flow in the circle of Willis: modeling and calibration. *Multiscale Model. Simul.*, 7:888–909, 2008.
- [60] D. Bessems, C.G. Giannopapa, M.C.M. Rutten, and F.N. van de Vosse. Experimental validation of a time-domain-based wave propagation model of blood flow in viscoelastic vessels. *J. Biomech.*, 41:284–291, 2008.
- [61] D. Valdez-Jasso, M.A. Haider, H.T. Banks, D.B. Santana, Y.Z. German, R.L. Armentano, and M.S. Olufsen. Analysis of viscoelastic wall properties in ovine arteries. *IEEE Trans. Biomed. Eng.*, 56:210–219, 2009.
- [62] D. Valdez-Jasso, D. Bia, Y. Zócalo, R.L. Armentano, M.A. Haider, and M.S. Olufsen. Linear and nonlinear viscoelastic modeling of aorta and carotid pressure–area dynamics under *in vivo* and *ex vivo* conditions. *Annals Biomed. Eng.*, 39:1438–1456, 2011.
- [63] D.N. Ku. Blood flow in arteries. *Ann. Rev. Fluid Mech.*, 29:399–434, 1997.
- [64] A.I. Moens. Over de voortplantingssnelheid von den pols (on the speed of propagation of the pulse). *Technical report, Leiden*, pages 814–823, 1877.
- [65] D.J. Korteweg. Über die Fortpflanzungsgeschwindigkeit des Schalles in elastischen Röhern. *Ann. Phys. Chem. (NS)*, 5:525–527, 1878.
- [66] J.J. Wang and K.H. Parker. Wave propagation in a model of the arterial circulation. *J. Biomech.*, 37:457–470, 2004.
- [67] B.N. Steele, J. Wan, J.P. Ku, T.J.R. Hughes, and C.A. Taylor. *In vivo* validation of a one-dimensional finite-element method for predicting blood flow in cardiovascular bypass grafts. *IEEE Trans. Biomed. Eng.*, 50:649–656, 2003.
- [68] J.P. Mynard and P. Nithiarasu. A 1D arterial blood flow model incorporating ventricular pressure, aortic valve and regional coronary flow using the locally conservative Galerkin (LCG) method. *Commun. Numer. Meth. Eng.*, 24:367–417, 2008.
- [69] J.E. Davies, Z.I. Whinnett, D.P. Francis, C.H. Manisty, J. Aguado-Sierra, K. Willson, R.A. Foale, I.S. Malik, A.D. Hughes, K.H. Parker, and J. Mayet. Evidence of a dominant backward-propagating “suction” wave responsible for diastolic coronary filling in humans, attenuated in left ventricular hypertrophy. *Circulation*, 113:1768–1778, 2006.

- [70] J. Spaan, C. Kolyva, J. van den Wijngaard, R. ter Wee, P. van Horseen, J. Piek, and M. Siebes. Coronary structure and perfusion in health and disease. *Phil. Trans. Roy. Soc. A*, 366:3137–3153, 2008.
- [71] L. Formaggia, D. Lamponi, M. Tuveri, and A. Veneziani. Numerical modeling of 1D arterial networks coupled with a lumped parameters description of the heart. *Comp. Meth. Biomech. Biomed. Eng.*, 9:273–288, 2006.
- [72] J. Alastruey, K.H. Parker, J. Peiró, S.M. Byrd, and S.J. Sherwin. Modelling the circle of Willis to assess the effects of anatomical variations and occlusions on cerebral flows. *J. Biomech.*, 40:1794–1805, 2007.
- [73] J. Alastruey, K.H. Parker, J. Peiró, and S.J. Sherwin. Can the modified Allen’s test always detect sufficient collateral flow in the hand? A computational study. *Comp. Meths. Biomech. Biomed. Eng.*, 9:353–361, 2006.
- [74] M. Willemet. *Blood Flow Modeling for Patient-Specific Bypass Surgery in Lower-Limb Arteries*. PhD thesis, Université catholique de Louvain, Belgium, 2012.
- [75] K.S. Matthys, J. Alastruey, J. Peiró, A.W. Khir, P. Segers, P.R. Verdonck, K.H. Parker, and S.J. Sherwin. Pulse wave propagation in a model human arterial network: Assessment of 1-D numerical simulations against *in vitro* measurements. *J. Biomech.*, 40:3476–3486, 2007.
- [76] J.-J. Wang, J.A. Flewitt, N.G. Shrive, K.H. Parker, and J.V. Tyberg. Systemic venous circulation. Waves propagating on a windkessel: relation of arterial and venous windkessels to systemic vascular resistance. *Am. J. Heart Circ. Physiol.*, 290:H154–H162, 2006.
- [77] J. Alastruey, S.M. Moore, K.H. Parker, T. David, J. Peiró, and S.J. Sherwin. Reduced modelling of blood flow in the cerebral circulation: Coupling 1-D, 0-D and cerebral auto-regulation models. *Int. J. Numer. Meth. Fluids*, 56:1061–1067, 2008.
- [78] D.J. Brown. Input impedance and reflection coefficient in fractal-like models of asymmetrically branching compliant tubes. *IEEE Trans. Biomed. Eng.*, 43:715–722, 1996.
- [79] M.S. Olufsen. Structured tree outflow condition for blood flow in larger systemic arteries. *Am. J. Physiol.*, 276:H257–H268, 1999.
- [80] A. Quarteroni, S. Ragni, and A. Veneziani. Coupling between lumped and distributed models for blood flow problems. *Comput. Visual. Sci.*, 4:111–124, 2001.
- [81] F.Y. Liang, S. Takagi, R. Himeno, and H. Liu. Biomechanical characterization of ventricular–arterial coupling during aging: A multi-scale model study. *J. Biomech.*, 42:692–704, 2009.
- [82] J.C. Stettler, P. Niederer, and M. Anliker. Theoretical analysis of arterial hemodynamics including the influence of bifurcations. Part II: Critical evaluation of theoretical model and comparison with noninvasive measurements of flow patterns in normal and pathological cases. *Ann. Biomed. Eng.*, 9:165–175, 1981.
- [83] P. Reymond, Y. Bohraus, F. Perren, F. Lazeyras, and N. Stergiopulos. Validation of a patient-specific one-dimensional model of the systemic arterial tree. *Am. J. Physiol. Heart Circ. Physiol.*, 301:H1173–H1182, 2011.
- [84] P. Segers, F. Dubois, D. De Wachter, and P. Verdonck. Role and relevancy of a cardiovascular simulator. *Cardiov. Engng.*, 3:48–56, 1998.
- [85] W. Huberts, K. Van Canneyt, P. Segers, S. Eloot, J.H.M. Tordoir, P. Verdonck, F.N. van de Vosse, and E.M.H. Bosboom. Experimental validation of a pulse wave propagation model for predicting hemodynamics after vascular access surgery. *J. Biomech.*, 45:1684–1691, 2012.
- [86] J. Alastruey, S.R. Nagel, B. Nier, A.A.E Hunt, P.D. Weinberg, and J. Peiró. Modelling pulse wave propagation in the rabbit systemic circulation to assess the effects of altered nitric oxide synthesis. *J. Biomech.*, 42:2116–2123, 2009.
- [87] C.A. Taylor and C.A. Figueroa. Patient-specific modeling of cardiovascular mechanics. *Annu. Rev. Biomed. Eng.*, 11:109–134, 2009.
- [88] E-S. H. Ibrahim, K.R. Johnson, A.B. Miller, J.M. Shaffer, and R.D. White. Measuring aortic pulse wave velocity using high-field cardiovascular magnetic resonance: comparison of techniques. *J. Cardiov. Magn. Reson.*, 12:26–39, 2010.
- [89] C. Oates. *Cardiovascular Haemodynamics and Doppler Waveforms Explained*. Greenwich Medical Media LTD, 2001.
- [90] A.C. Simon, M.E. Safar, J.A. Levenson, G.M. London, B.I. Levy, and N.P. Chau. An evaluation of large arteries compliance in man. *Am. J. Physiol.*, 237:H550–H554, 1979.
- [91] J.P. Murgo, N. Westerhof, J.P. Giolma, and S.A. Altobelli. Aortic input impedance in normal man: relationship to pressure wave forms. *Circulation*, 62:105–116, 1980.
- [92] R.D. Latham, N. Westerhof, P. Sipkema, B.J. Rubal, P. Reuderink, and J.P. Murgo. Regional wave travel and reflections along the human aorta. *Circulation*, 72:1257–1269, 1985.
- [93] D.W. Holdsworth, C.J.D. Norley, R. Frayne, D.A. Steinman, and B.K. Rutt. Characterization of common carotid artery blood-flow waveforms in normal human subjects. *Physiol. Meas.*, 20:219–240, 1999.

- [94] C.P. Cheng, R.J. Herfkens, and C.A. Taylor. Abdominal aortic hemodynamic conditions in healthy subjects aged 50–70 at rest and during lower limb exercise: in vivo quantification using MRI. *Atherosclerosis*, 168:323–331, 2003.
- [95] A.P. Avolio, S. Chen, R. Wang, C. Zhang, M. Li, and M.F. O’Rourke. Effects of aging on changing arterial compliance and left ventricular load in a northern chinese urban community. *Circulation*, 68:50–58, 1983.
- [96] A.W. Feinberg and H. Lax. Studies of the arterial pulse wave. *Circulation*, 18:1125–1130, 1958.
- [97] N. Stergiopulos, D.F. Young, and T.R. Rogge. Computer simulation of arterial flow with applications to arterial and aortic stenoses. *J. Biomech.*, 25:1477–1488, 1992.
- [98] P.J. Chowienzyk, R. Kelly, H. MacCallum, S.C. Millasseau, T. Andersson, R.G. Gosling, J.M. Ritter, and E.E. Änggård. Photoplethysmographic assessment of pulse wave reflection: blunted response to endothelium-dependent β_2 -adrenergic vasodilation in type 2 diabetes. *J. Am. Coll. Cardiol.*, 34:2007–2014, 1999.
- [99] N. Westerhof and G. Elzinga. Normalized input impedance and arterial decay time over heart period are independent of animal size. *Am. J. Physiol. Regul. Integr. Comp. Physiol.*, 261:R126–R133, 1991.
- [100] K.H. Parker and C.J.H. Jones. Forward and backward running waves in the arteries: analysis using the method of characteristics. *J. Biomech. Eng.*, 112:322–326, 1990.
- [101] J. Alastruey, T. Passerini, L. Formaggia, and J. Peiró. Physical determining factors of the arterial pulse waveform: theoretical analysis and estimation using the 1-D formulation. *J. Eng. Math. (online first)*, 2012.
- [102] C.D. Bertram, F. Pythoud, N. Stergiopulos, and J.-J. Meister. Pulse wave attenuation measurement by linear and nonlinear methods in nonlinearly elastic tubes. *Med. Eng. Phys.*, 21:155–166, 1999.
- [103] M. Anliker, M.B. Hstand, and E. Ogden. Dispersion and attenuation of small artificial pressure waves in the canine aorta. *Circ. Res.*, 23:539–551, 1968.
- [104] P. Segers, N. Stergiopulos, P. Verdonck, and R. Verhoeven. Assessment of distributed arterial network models. *Med. Bio. Eng. Comput.*, 35:729–736, 1997.
- [105] V. Milišić and A. Quarteroni. Analysis of lumped parameter models for blood flow simulations and their relation with 1D models. *Mathem. Mod. and Num. Analysis*, 38:613–632, 2004.
- [106] A.P. Avolio. Multi-branched model of the human arterial system. *Med. and Biol. Engng. and Comput.*, 18:709–718, 1980.
- [107] W. Huberts, E.M.H. Bosboom, and F.N. van de Vosse. A lumped model for blood flow and pressure in the systemic arteries based on an approximate velocity profile function. *Math. Biosciences Eng.*, 6(27–40), 2009.
- [108] B.J.B.M. Wolters, M. Emmera, M.C.M. Rutten, G.W.H. Schurink, and F.N. van de Vosse. Assessment of endoleak significance after endovascular repair of abdominal aortic aneurysms: A lumped parameter model. *Med. Eng. Phys.*, 29:1106–1118, 2007.
- [109] N. Westerhof, F. Bosman, C.J. de Vries, and A. Noordergraaf. Analog studies of the human systemic arterial tree. *J. Biomech.*, 2:121–143, 1969.
- [110] O. Frank. Die Grundform des arteriellen Pulses. *Erste Abhandlung Mathematische Analyse Z Biol*, 37:483–526, 1899.
- [111] N. Stergiopulos, B.E. Westerhof, and N. Westerhof. Total arterial inertance as the fourth element of the windkessel model. *Am. J. Physiol.*, 276:H81–H88, 1999.
- [112] M. Danielsen and J.T. Ottesen. A cardiovascular model. In J.T. Ottesen, M.S. Olufsen, and J.K. Larsen, editors, *Applied Mathematical Models in Human Physiology*. SIAM monographs on mathematical human physiology, Philadelphia, 2004.
- [113] G.L. Papageorgiou and N.B. Jones. Arterial system configuration and wave reflection. *J. Biomed. Eng.*, 9:299–301, 1987.
- [114] G.L. Papageorgiou, B.N. Jones, V.J. Redding, and N. Hudson. The area ratio of normal arterial junctions and its implications in pulse wave reflections. *Cardiov. Res.*, 24:478–484, 1990.
- [115] J.E. Davies, J. Alastruey, D.P. Francis, N. Hadjiloizou, Z.I. Whinnett, C.H. Manisty, J. Aguado-Sierra, K. Willson, R.A. Foale, I.S. Malik, A.D. Hughes, K.H. Parker, and J. Mayet. Attenuation of wave reflection by wave entrapment creates an ‘horizon effect’ in the human aorta. *Hypertension (accepted)*, 2012.
- [116] J. Alastruey, K.H. Parker, J. Peiró, and S.J. Sherwin. Lumped parameter outflow models for 1-D blood flow simulations: Effect on pulse waves and parameter estimation. *Commun. Comput. Phys.*, 4:317–336, 2008.
- [117] J. Alastruey, K.H. Parker, J. Peiró, and S.J. Sherwin. Analysing the pattern of pulse waves in arterial networks: a time-domain study. *J. Eng. Math.*, 64:331–351, 2009.
- [118] N. Stergiopulos, M. Spiridon, F. Pythoud, and J.-J. Meister. On the wave transmission and reflection properties of stenoses. *J. Biomech.*, 29:31–38, 1996.
- [119] A. Swillens, L. Lanoye, J. De Backer, N. Stergiopulos, P.R. Verdonck, F. Vermassen, and P. Segers. Effect of an abdominal aortic aneurysm on wave reflection in the aorta. *IEEE Trans. Biomed. Eng.*, 55:1602–1611, 2008.

- [120] J.-J. Wang, A.B. O'Brien, N.G. Shrive, K.H. Parker, and J.V. Tyberg. Time-domain representation of ventricular-arterial coupling as a windkessel and wave system. *Am. J. Physiol. Heart Circ. Physiol.*, 284:H1358–H1368, 2003.
- [121] J. Aguado-Sierra, J. Alastruey, J.-J. Wang, N. Hadjiloizou, J.E. Davies, and K.H. Parker. Separation of the reservoir and wave pressure and velocity from measurements at an arbitrary location in arteries. *Proc. Inst. Mech. Eng., Part H, J. Eng. Med.*, 222:403–416, 2008.
- [122] G.F. Mitchell, L.A. Moyé, E. Braunwald, J.-L. Rouleau, V. Bernstein, E.M. Geltman, G.C. Flaker, and M.A. Pfeffer and SAVE Investigators. Sphygmomanometrically determined pulse pressure is a powerful independent predictor of recurrent events after myocardial infarction in patients with impaired left ventricular function. *Circulation*, 96:4254–4260, 1997.
- [123] A. Benetos, M. Safar, A. Rudnichi, H. Smulyan, J.L. Richard, P. Ducimetière, and L. Guize. Pulse pressure: A predictor of long-term cardiovascular mortality in a French male population. *Hypertension*, 30:1410–1415, 1997.
- [124] S.S. Franklin, S.A. Khan, N.D. Wong, M.G. Larson, and D. Levy. Is pulse pressure useful in predicting risk for coronary heart disease? The Framingham Heart Study. *Circulation*, 100:354–360, 1999.
- [125] J.R. Cockcroft, I.B. Wilkinson, M. Evans, P. McEwan, J.R. Peters, S. Davies, M.F. Scanlon, and C.J. Currie. Pulse pressure predicts cardiovascular risk in patients with Type 2 diabetes mellitus. *Am. J. Hypert.*, 18:1463–1467, 2005.
- [126] M.E. Safar, J. Blacher, and P. Jankowski. Arterial stiffness, pulse pressure, and cardiovascular disease – Is it possible to break the vicious circle? *Atherosclerosis*, 218:263–271, 2011.
- [127] M.F. O'Rourke, T. Yaginuma, and A.P. Avolio. Physiological and pathological implications of ventricular/vascular coupling. *Annals Biomed. Eng.*, 12:119–134, 1984.
- [128] J. Alastruey. On the mechanics underlying the reservoir–excess separation in systemic arteries and their implications for pulse wave analysis. *Cardiov. Eng.*, 10:176–189, 2010.
- [129] A. Zambanini, S.L. Cunningham, K.H. Parker, A.W. Khir, S.A. McG. Thom, and A.D. Hughes. Wave-energy patterns in carotid, brachial, and radial arteries: a noninvasive approach using wave-intensity analysis. *Am. J. Physiol. Heart Circ. Physiol.*, 289:H270–H276, 2005.
- [130] J.E. Davies, Z.I. Whinnett, D.P. Francis, K. Willson, R.A. Foale, I.S. Malik, A.D. Hughes, K.H. Parker, and J. Mayet. Use of simultaneous pressure and velocity measurements to estimate arterial wave speed at a single site in humans. *Am. J. Physiol. Heart Circ. Physiol.*, 290:H878–H885, 2006.
- [131] J.A. Levenson, P.P. Peronneau, A.C. Simon, and M.E. Safar. Pulsed Doppler: Determination of diameter, blood flow velocity and volumic flow of brachial artery in man. *Cardiov. Res.*, 15:164–170, 1981.
- [132] A.D. Hughes and K.H. Parker. Forward and backward waves in the arterial system: impedance or wave intensity analysis? *Med. Bio. Eng. Comput.*, 47:207–210, 2009.
- [133] F. Pythoud, N. Stergiopulos, and J.-J. Meister. Separation of arterial pressure waves into their forward and backward running components. *J. Biomech. Eng.*, 118:295–301, 1996.
- [134] N. Westerhof, P. Sipkema, G. Van Den Bos, and G. Elzinga. Forward and backward waves in the arterial system. *Cardiov. Res.*, 6:648–656, 1972.
- [135] N. Westerhof, N. Stergiopulos, and M.I.M. Noble. *Snapshots of Hemodynamics: An Aid for Clinical Research and Graduate Education*. Springer (New York), 2005.
- [136] J.E. Davies, N. Hadjiloizou, D. Leibovich, A. Malaweera, J. Alastruey, Z.I. Whinnett, C.H. Manisty, D.P. Francis, J. Aguado-Sierra, R.A. Foale, I.S. Malik, K.H. Parker, J. Mayet, and A.D. Hughes. Importance of the aortic reservoir in determining the shape of the arterial pressure waveform – The forgotten lessons of Frank. *Artery Research*, 1:40–45, 2007.
- [137] J.E. Davies, P.S. Lacy, K. Cruickshank, A. Stanton, D. Collier, H. Thurston, B. Williams, K.H. Parker, S.M. Thom, and A.D. Hughes. Excess pressure is higher in atenolol-treated individuals and independently predicts cardiovascular events in the CAFE substudy of ASCOT. *Eur Heart J 31 (Abstract Supplement):902*, 2010.
- [138] P. Jankowski, K. Kawecka-Jaszcz, D. Czarnecka, M. Brzozowska-Kiszka, K. Styczkiewicz, M. Styczkiewicz, A. Pośnik-Urbańska, L. Bryniarski, and D. Dudek. Ascending aortic, but not brachial blood pressure-derived indices are related to coronary atherosclerosis. *Atherosclerosis*, 176:151–155, 2004.
- [139] B. Williams, P.S. Lacy, S.M. Thom, K. Cruickshank, A. Stanton, D. Collier, A.D. Hughes, H. Thurston, M. O'Rourke, CAFE Investigators, Anglo-Scandinavian Cardiac Outcomes Trial Investigators, and CAFE Steering Committee and Writing Committee. Differential impact of blood pressure-lowering drugs on central aortic pressure and clinical outcomes. Principal results of the Conduit Artery Function Evaluation (CAFE) study. *Circulation*, 113:1213–1225, 2006.
- [140] M. Karamanoglu, D.E. Gallagher, A.P. Avolio, and M.F. O'Rourke. Pressure wave propagation in a multi-branched model of the human upper limb. *Am. J. Physiol.*, 269:H1363–H1369, 1995.

- [141] N. Stergiopulos, B.E. Westerhof, and N. Westerhof. Physical basis of pressure transfer from periphery to aorta: a model-based study. *Am. J. Physiol. Heart Circ. Physiol.*, 274:H1386–H1392, 1998.
- [142] B.E. Westerhof, I. Guelen, W.J. Stok, K.H. Wesseling, J.A. Spaan, N. Westerhof, W.J. Bos, and N. Stergiopulos. Arterial pressure transfer characteristics: effects of travel time. *Am. J. Physiol. Heart Circ. Physiol.*, 292:H800–H807, 2007.
- [143] K.H. Parker. An introduction to wave intensity analysis. *Med. Bio. Eng. Comput.*, 47:175–188, 2009.
- [144] C.J.H. Jones, K.H. Parker, R. Hughes, and D.J. Sheridan. Nonlinearity of human arterial pulse wave transmission. *Trans. ASME J. Biomech. Eng.*, 114:10–14, 1992.
- [145] C.J.H. Jones and M. Sugawara. "Wavefront" in the aorta – implications for the mechanisms of left ventricular ejection and aortic valve closure. *Cardiov. Res.*, 27:1902–1905, 1993.
- [146] A.W. Khir, M.Y. Henein, T. Koh, S.K. Das, K.H. Parker, and D.G. Gibson. Arterial waves in humans during peripheral vascular surgery. *Clin. Sci.*, 101:749–757, 2001.
- [147] C.J.H. Jones, M. Sugawara, Y. Kondoh, K. Uchida, and K.H. Parker. Compression and expansion wavefront travel in canine ascending aortic flow: wave intensity analysis. *Heart Vessels*, 16:91–98, 2002.
- [148] N. Ohte, H. Narita, M. Sugawara, K. Niki, T. Okada, A. Harada, J. Hayano, and G. Kimura. Clinical usefulness of carotid arterial wave intensity in assessing left ventricular systolic and early diastolic performance. *Heart Vessels*, 18:107–111, 2003.
- [149] Y.H. Sun, T.J. Anderson, K.H. Parker, and J.V. Tyberg. Wave-intensity analysis: a new approach to coronary hemodynamics. *J. Applied Physiol.*, 89:1636–1644, 2000.
- [150] D.J. Penny, J.P. Mynard, and J.J. Smolich. Aortic wave intensity analysis of ventricular-vascular interaction during incremental dobutamine infusion in adult sheep. *Am. J. Physiol. Heart Circ. Physiol.*, 294:H481–H489, 2008.
- [151] V. Martin, F. Clément, A. Decoene, and J.F. Gerbeau. Parameter identification for a one-dimensional blood flow model. *ESAIM: Proc.*, 14:174–200, 2005.
- [152] C.A.D. Leguy, E.M.H. Bosboom, H. Gelderblom, A.P.G. Hoeks, and F.N. van de Vosse. Estimation of distributed arterial mechanical properties using a wave propagation model in a reverse way. *Med. Eng. Phys.*, 32:957–967, 2010.
- [153] A.W. Khir, A. O'Brien, J.S.R. Gibbs, and K.H. Parker. Determination of wave speed and wave separation in the arteries. *J. Biomech.*, 34:1145–1155, 2001.
- [154] K.H. Wesseling, J.R. Jansen, J.J. Settels, and J.J. Schreuder. Computation of aortic flow from pressure in humans using a nonlinear, three-element model. *J. Appl. Physiol.*, 74:2566–2573, 1993.
- [155] P. Segers, E.R. Rietzschel, M.L. De Buyzere, N. Stergiopulos, N. Westerhof, L.M. Van Bortel, T. Gillebert, and P.R. Verdonck. Three- and four-element Windkessel models: assessment of their fitting performance in a large cohort of healthy middle-aged individuals. *Proc. Inst. Mech. Eng., Part H, J. Eng. Med.*, 222:417–428, 2008.
- [156] E. Hermeling, A.P.G. Hoeks, M.H.M. Winkens, J.L. Waltenberger, R.S. Reneman, A.A. Kroon, and K.D. Reesink. Noninvasive assessment of arterial stiffness should discriminate between systolic and diastolic pressure ranges. *Hypertension*, 55:124–130, 2010.
- [157] A.P.G. Hoeks, J.M. Willigers, and R.S. Reneman. Effects of assessment and processing techniques on the shape of arterial pressure-distension loops. *J. Vasc. Res.*, 37:494–500, 2000.
- [158] B. Trachet, P. Reymond, J. Kips, A. Swillens, M. De Buyzere, B. Suys, N. Stergiopulos, and P. Segers. Numerical validation of a new method to assess aortic pulse wave velocity from a single recording of a brachial artery waveform with an occluding cuff. *Annals Biomed. Eng.*, 38:876–888, 2010.
- [159] J. Alastruey. Numerical assessment of time-domain methods for the estimation of local arterial pulse wave speed. *J. Biomech.*, 44:885–891, 2011.
- [160] N. Stergiopulos, J.-J. Meister, and N. Westerhof. Evaluation of methods for estimation of total arterial compliance. *Am. J. Physiol. Heart Circ. Physiol.*, 37:H1540–H1548, 1995.
- [161] X. Xiao, E.D. Ozawa, Y. Huang, and R.D. Kamm. Model-based assessment of cardiovascular health from noninvasive measurements. *Annals Biomed. Eng.*, 30:612–623, 2002.
- [162] F. Cassot, M. Zagzoule, and J.P. Marc-Vergnes. Hemodynamic role of the circle of Willis in stenoses of internal carotid arteries. An analytical solution of a linear model. *J. Biomech.*, 33:395–405, 2000.
- [163] M. Karamanoglu, M.F. O'Rourke, A.P. Avolio, and R.P. Kelly. An analysis of the relationship between central aortic and peripheral upper limb pressure waves in man. *Eur. Heart J.*, 14:160–167, 1993.
- [164] P. Segers, A. Qasem, T. De Backer, S. Carlier, P. Verdonck, and A. Avolio. Peripheral 'oscillatory' compliance is associated with aortic augmentation index. *Hypertension*, 37:1434–1439, 2001.
- [165] R.H. Kufahl and M.E. Clark. A circle of Willis simulation using distensible vessels and pulsatile flow. *J. Biomech. Eng.*, 107:112–123, 1985.

- [166] B. Hillen, H.W. Hoogstraten, and L. Post. A mathematical model of the flow in the circle of Willis. *J. Biomech.*, 19:187–194, 1986.
- [167] J. Wan, B. Steele, S.A. Spicer, S. Strohband, G.R. Feijóo, T.J.R. Hughes, and C.A. Taylor. A one-dimensional finite element method for simulation-based medical planning for cardiovascular disease. *Comp. Meths. Biomech. Biomed. Eng.*, 5:195–206, 2002.
- [168] E. Marchandise, M. Willemet, and V. Lacroix. A numerical hemodynamic tool for predictive vascular surgery. *Med. Eng. Phys.*, 31:131–144, 2009.
- [169] C.A. Taylor, M.T. Draney, J.P. Ku, D. Parker, B.N. Steele, K. Wang, and C.K. Zarins. Predictive medicine: Computational techniques in therapeutic decision-making. *Computer Aided Surgery*, 4:231–247, 1999.
- [170] W. Huberts, E.M.H. Bosboom, R.N. Planken, J.H.M. Tordoir, and F.N. van de Vosse. Patient-specific computational modeling to improve the clinical outcome of vascular access creation. In J.H.M. Tordoir, editor, *Vascular Access*, pages 51–63. Ed. Minerva Med., 2009.
- [171] W. Huberts, A.S. Bode, W. Kroon, R.N. Planken, J.H.M. Tordoir, F.N. van de Vosse, and E.M.H. Bosboom. A pulse wave propagation model to support decision-making in vascular access planning in the clinic. *Med. Eng. Phys.*, 34:233–248, 2012.
- [172] E. Marchandise and P. Flaud. Accurate modelling of unsteady flows in collapsible tubes. *Comp. Meths. Biomech. Biomed. Eng.*, 13:279–290, 2010.
- [173] K. Perktold, M. Resch, and R. Peter. 3-D numerical analysis of pulsatile flow and wall shear stress in the carotid artery bifurcation. *J. Biomech.*, 24:409–420, 1991.
- [174] S. Dong, J. Insley, N.T. Karonis, M.E. Papka, J. Binns, and G. Karniadakis. Simulating and visualizing the human arterial system on the TeraGrid. *Future Gener. Comput. Syst.*, 22:1011–1017, 2006.
- [175] L. Grinberg, T. Anor, J. Madsen, A. Yakhot, and G.E. Karniadakis. Large-scale simulation of the human arterial tree. *Clin. Exp. Pharm. Physiol.*, 36:194–205, 2009.
- [176] P.E. Vincent, A.M. Plata, A.A.E. Hunt, P.D. Weinberg, and S.J. Sherwin. Blood flow in the rabbit aortic arch and descending thoracic aorta. *J. R. Soc. Interface*, 8:1708–1719, 2011.
- [177] S.A. Urquiza, P.J. Blanco, M.J. Vénere, and R.A. Feijóo. Multidimensional modelling for the carotid artery blood flow. *Comp. Meth. App. Mech. Eng.*, 195:4002–4017, 2006.
- [178] I.E. Vignon-Clementel, C.A. Figueroa, K.E. Jansen, and C.A. Taylor. Outflow boundary conditions for three-dimensional finite element modeling of blood flow and pressure in arteries. *Comp. Meth. App. Mech. Eng.*, 195:3776–3796, 2006.
- [179] G. Papadakis. Coupling 3D and 1D fluid–structure-interaction models for wave propagation in flexible vessels using a finite volume pressure-correction scheme. *Commun. Numer. Meth. Engng.*, 25:533–551, 2009.
- [180] B.W.A.M.M. Beulen, M.C.M. Rutten, and F.N. van de Vosse. A time-periodic approach for fluid-structure interaction in distensible vessels. *J. Fluids Struct.*, 25:954–966, 2009.
- [181] H. Ho, G. Sands, H. Schmid, K. Mithraratne, G. Mallinson, and P. Hunter. A hybrid 1D and 3D approach to hemodynamics modelling for a patient-specific cerebral vasculature and aneurysm. *Med. Image Comput. Comput. Assist. Interv.*, 12(323–330), 2009.
- [182] T. Passerini, M.R. De Luca, L. Formaggia, A. Quarteroni, and A. Veneziani. A 3D/1D geometrical multiscale model of cerebral vasculature. *J. Eng. Math.*, 64:319–330, 2009.
- [183] M. Ursino. Interaction between carotid baroregulation and the pulsating heart: a mathematical model. *Am. J. Heart Circ. Physiol.*, 275:H1733–H1747, 1998.
- [184] B. Cockburn and C-W. Shu. The local discontinuous Galerkin method for time-dependent convection-diffusion systems. *SIAM J. Num. Anal.*, 35:2440–2463, 1998.
- [185] O.C. Zienkiewicz, R.L. Taylor, S.J. Sherwin, and J. Peiró. On discontinuous Galerkin methods. *Int. J. Numer. Meth. Eng.*, 58(2):1119–1148, 2003.
- [186] G.E. Karniadakis and S.J. Sherwin. *Spectral/hp Element Methods for Computational Fluid Dynamics*. Oxford University Press, 2005.
- [187] B.S. Brook, S.A.E.G. Falle, and T.J. Pedley. Numerical solutions for unsteady gravity-driven flows in collapsible tubes: evolution and roll-wave instability of a steady state. *J. Fluid Mech.*, 396:223–256, 1999.
- [188] E.F. Toro and A. Siviglia. Simplified blood flow model with discontinuous vessel properties: analysis and exact solutions. In D. Ambrosi and A. Quarteroni and G. Rozza, editor, *Modelling Physiological Flows*. Springer, 2011.
- [189] M.A. Fernández, V. Milišić, and A. Quarteroni. Analysis of a geometrical multiscale blood flow model based on the coupling of ODE’s and hyperbolic PDE’s. *SIAM J. Multiscale Mod. Sim.*, 4:215–236, 2005.

Appendix 1: Nomenclature and abbreviations

Table 5: Nomenclature, abbreviations and SI units. Units commonly used in the clinic that are different from SI units are also shown after a semicolon.

A	(m ² ; cm ² or mm ²)	luminal cross-sectional area
A_0	(m ²)	luminal cross-sectional area at pressure P_{ext}
A_{ref}	(m ²)	reference area used to calculate A_0
a	(m ²)	linear perturbation of the luminal cross-sectional area
\mathcal{A}		tube law relating P and A
C	(m ³ Pa ⁻¹ ; mL mmHg ⁻¹)	compliance of the peripheral RCR Windkessel model
C_{0D}	(m ³ Pa ⁻¹)	elastic wall compliance within an arterial segment
C_{1D}	(m ² Pa ⁻¹)	elastic wall compliance per unit length of vessel
C_T	(m ² Pa ⁻¹)	total arterial compliance
$C_{f,b}$		forward and backward characteristic paths
C_c, C_p	(m ² Pa ⁻¹)	total conduit and peripheral compliance, respectively
c	(m s ⁻¹)	pulse wave speed
c_0	(m s ⁻¹)	pulse wave speed at pressure P_{ext}
CT		computer tomography
dI	(W m ⁻²)	wave intensity
dP	(Pa)	change of pressure across a wavefront
dU	(m s ⁻¹)	change of velocity across a wavefront
E	(Pa)	Young's modulus of the arterial wall
$\mathbf{F}, \mathbf{F}_e, \mathbf{F}_v$		total, elastic and viscous vector of fluxes, respectively
$\mathbf{F}^*, \mathbf{F}_e^*, \mathbf{F}_v^*$		approximation of the total, elastic and viscous vector of fluxes, respectively, at the numerical interfaces
f	(N m ⁻¹)	frictional force per unit length of length
h	(m; mm)	vessel wall thickness
J_e	(m)	Jacobian of the elemental mapping from Ω_{st} to Ω_e
IVUS		intravascular ultrasound
L_{0D}	(kg m ⁻⁵)	blood inertia within an arterial domain
L_{1D}	(kg m ⁻⁶)	blood inertia per unit length of vessel
L_j		Legendre polynomial used in the discontinuous Galerkin scheme
l	(m; cm)	length of an arterial segment
M		total number of terminal branches in the arterial network
MR		magnetic resonance
N		total number of arterial segments (or edges) in the arterial network
N_{el}		number of elemental regions Ω_e in the numerical mesh of an arterial segment
P	(Pa; mmHg)	average internal blood pressure over the luminal cross section
$P_{\text{con}}, P_{\text{per}}$	(Pa; mmHg)	conduit and peripheral components of blood pressure, respectively
P_d	(Pa; mmHg)	diastolic pressure
P_e	(Pa; mmHg)	elastic component of blood pressure
$P_{\text{exc}}, P_{\text{res}}$	(Pa; mmHg)	excess and reservoir components of blood pressure, respectively
P_{ext}	(Pa; mmHg)	external (or extramural) pressure
P_f, P_b	(Pa; mmHg)	forward and backward components of blood pressure, respectively
P_{out}	(Pa; mmHg)	blood pressure at which flow to the microcirculation ceases
P_{ref}	(Pa; mmHg)	reference blood pressure used to calculate A_0
p, p_e	(Pa)	linear perturbation of the total and elastic blood pressure, respectively
\tilde{p}_e	(Pa)	space-averaged elastic pressure within an arterial segment
$p_{\text{e in}}, p_{\text{e out}}$	(Pa)	linear perturbation of the elastic blood pressure at the inlet and outlet of the arterial domain, respectively

Table 6: Continuation of nomenclature, abbreviations and units.

p_w	(Pa)	space-independent (Windkessel) blood pressure
\mathcal{P}		polynomial order of the expansion bases in the discontinuous Galerkin scheme
Q	($\text{m}^3 \text{ s}^{-1}$; mL s^{-1} or L min^{-1})	blood volume flow rate
$Q_{\text{con}}, Q_{\text{per}}$	($\text{m}^3 \text{ s}^{-1}$)	conduit and peripheral components of the flow rate, respectively
\overline{Q}_{in}	($\text{m}^3 \text{ s}^{-1}$; mL s^{-1} or L min^{-1})	blood volume flow rate at the inlet of the ascending aorta
\overline{Q}_{in}	($\text{m}^3 \text{ s}^{-1}$; mL s^{-1} or L min^{-1})	cardiac output generated by the left ventricle
q	($\text{m}^3 \text{ s}^{-1}$)	linear perturbation of the blood volume flow rate
\tilde{q}_e	($\text{m}^3 \text{ s}^{-1}$)	space-averaged blood volume flow rate within an arterial segment
$q_{\text{in}}, q_{\text{out}}$	(m^3)	linear perturbation of the volume flow rate at the inlet and outlet of the arterial domain, respectively
\mathcal{Q}		order of the Gauss quadrature used in the numerical solution
R_1, R_2	(Pa s m^{-3})	inflow and outflow resistance of the peripheral RCR Windkessel model, respectively
R_{0D}	(Pa s m^{-3})	resistance within an arterial segment due to blood viscosity
R_{1D}	(Pa s m^{-4})	resistance per unit length of vessel due to blood viscosity
$R_f^{a,b,c}$		reflection coefficient in the parent and first and second daughter vessels, respectively, joining in a junction
R_T	(Pa s m^{-3} ; mmHg s mL^{-3})	net peripheral resistance of the arterial network
R_v		reflection coefficient at the aortic valve
\mathcal{R}	(m; cm)	luminal radius
\mathcal{R}_0	(m; cm)	luminal radius at pressure P_{ext}
r	(m)	radial coordinate in the luminal cross section
S	(m^2 ; cm^2 or mm^2)	luminal cross section
$\mathbf{S}, \hat{\mathbf{S}}$		source term vector in the non-conservative and conservative form, respectively
T	(s)	period of the heartbeat
$T^{a,b,c}$		transmission coefficient in the parent and first and second daughter vessels, respectively, joining in a junction
t	(s)	time
$\mathbf{U}, \mathbf{U}^\delta$		vector of unknowns in the discontinuous Galerkin scheme
U	(m s^{-1} ; cm s^{-1})	average axial blood velocity over the luminal cross section
U_f, U_b	(m s^{-1} ; cm s^{-1})	forward and backward components of blood velocity, respectively
U_0	(m s^{-1})	reference average axial blood velocity
u	(m s^{-1} ; cm s^{-1})	axial blood velocity of each fluid particle in the luminal cross-section
\mathbf{V}^δ		finite space of piecewise polynomial vector functions
$W_{f,b}$	(m s^{-1})	nonlinear forward and backward characteristic (or Riemann) variables
WSS	(Pa)	wall shear stress
$w_{f,b}$	($\text{m}^3 \text{ s}^{-1}$)	linear forward and backward characteristic (or Riemann) variables
x	(m)	axial coordinate of an arterial segment Ω
$\hat{x}(t)$		parametric function in the (x, t) space
x_e^l	(m)	axial coordinate of the lower point of the elemental region Ω_e
x_e^u	(m)	axial coordinate of the upper point of the elemental region Ω_e
Y_0	($\text{m Pa}^{-1} \text{ s}^{-1}$)	characteristic admittance of the vessel
Z_0	(Pa s m^{-3})	characteristic impedance of the vessel
α		flow profile constant or Coriolis coefficient
β	(Pa m)	parameter related to the wall elastic tone
Γ	(Pa s m)	parameter related to the wall viscosity
γ	(Pa s m^{-1})	parameter related to the wall viscosity in the linear model
Δt	(s)	time step of the numerical approximation
δ		arbitrary scaling factor used in the method of characteristics
ζ		parameter that defines the velocity profile
λ_f, λ_b	(m s^{-1})	forward and backward eigenvalues of the characteristic system
μ	(Pa s)	dynamic viscosity of blood
ξ		non-dimensional coordinate of the domain Ω_{st}
ρ	(kg m^{-3})	blood density
σ		surface coordinate in the cross section S
φ	(Pa s)	viscosity of the arterial wall
ψ		test functions in the discontinuous Galerkin scheme
Ω		1-D domain of an arterial segment
Ω_e		elemental region within Ω
Ω_{st}		reference (or standard) 1-D domain linked to Ω through an affine mapping

Appendix 2: Discontinuous Galerkin scheme

This is a convenient scheme for high-order discretisation of convection-dominated flows [184], such as arterial flows. It allows us to propagate waves of different frequencies without suffering from excessive dispersion and diffusion errors and enables a straightforward connection of arterial segments through their inlet and outlet boundary conditions to model the arterial network. Here we describe this scheme in detail.

Eqs. (2) and (4) can be written in the following conservative form

$$\begin{aligned} \frac{\partial \mathbf{U}}{\partial t} + \frac{\partial \mathbf{F}}{\partial x} &= \hat{\mathbf{S}}, \quad \mathbf{U} = \begin{bmatrix} A \\ U \end{bmatrix}, \quad \hat{\mathbf{S}} = \begin{bmatrix} 0 \\ \frac{f}{\rho A} \end{bmatrix}, \\ \mathbf{F} &= \mathbf{F}_e + \mathbf{F}_v = \begin{bmatrix} AU \\ \frac{U^2}{2} + \frac{P_e}{\rho} \end{bmatrix} + \begin{bmatrix} 0 \\ -\frac{\Gamma}{\rho A_0 \sqrt{A}} \frac{\partial(AU)}{\partial x} \end{bmatrix}, \end{aligned} \quad (24)$$

in which we have separated the flux \mathbf{F} into an elastic (\mathbf{F}_e) and a viscous (\mathbf{F}_v) term, and applied the mass conservation $\frac{\partial A}{\partial t} = -\frac{\partial(AU)}{\partial x}$ to change the time derivative to a spatial derivative in the viscous term of the tube law (4).

We discretise each arterial domain, $\Omega = [0, l]$, into a mesh of N_{el} non-overlapping elemental regions $\Omega_e = [x_e^l, x_e^u]$, $e = 1, \dots, N_{el}$, such that $x_e^u = x_{e+1}^l$, $e = 1, \dots, N_{el} - 1$, and $\bigcup_{e=1}^{N_{el}} \Omega_e = \Omega$. The superscripts l and u refer to the in and out boundaries of each Ω_e . Multiplying Eq. (24) by the test functions ψ and integrating over the domain Ω yields the weak form

$$\sum_{e=1}^{N_{el}} \left[\left(\frac{\partial \mathbf{U}}{\partial t}, \psi \right)_{\Omega_e} + \left(\frac{\partial \mathbf{F}}{\partial x}, \psi \right)_{\Omega_e} \right] = \sum_{e=1}^{N_{el}} (\hat{\mathbf{S}}, \psi)_{\Omega_e}, \quad (25)$$

where $(\mathbf{u}, \mathbf{v})_{\Omega} = \int_{\Omega} \mathbf{u} \mathbf{v} \, dx$ is the standard $\mathbf{L}^2(\Omega)$ inner product. Integration of the second term by parts leads to

$$\sum_{e=1}^{N_{el}} \left[\left(\frac{\partial \mathbf{U}}{\partial t}, \psi \right)_{\Omega_e} - \left(\mathbf{F}, \frac{d\psi}{dx} \right)_{\Omega_e} + [\mathbf{F} \cdot \psi]_{x_e^l}^{x_e^u} \right] = \sum_{e=1}^{N_{el}} (\hat{\mathbf{S}}, \psi)_{\Omega_e}. \quad (26)$$

Approximating \mathbf{U} and ψ by \mathbf{U}^{δ} and ψ^{δ} , respectively, which are in the finite space \mathbf{V}^{δ} of piecewise polynomial vector functions (they may be discontinuous across inter-element boundaries), integrating the second term in (26) once again by parts (to have a derivative on \mathbf{U}^{δ} rather than on ψ^{δ}), and denoting $\mathbf{F}^* = \mathbf{F}_e^* + \mathbf{F}_v^*$ as the approximation of the flux at the interface, we obtain the discrete form of our conservative law in the domain Ω in divergence form for all ψ^{δ} in \mathbf{V}^{δ} ,

$$\sum_{e=1}^{N_{el}} \left[\left(\frac{\partial \mathbf{U}^{\delta}}{\partial t}, \psi^{\delta} \right)_{\Omega_e} + \left(\frac{\partial \mathbf{F}(\mathbf{U}^{\delta})}{\partial x}, \psi^{\delta} \right)_{\Omega_e} + [\psi^{\delta} \cdot \{\mathbf{F}^* - \mathbf{F}(\mathbf{U}^{\delta})\}]_{x_e^l}^{x_e^u} \right] = \sum_{e=1}^{N_{el}} (\hat{\mathbf{S}}(\mathbf{U}^{\delta}), \psi^{\delta})_{\Omega_e}, \quad (27)$$

To obtain a global solution in the domain Ω , information must propagate between elemental regions Ω_e . This is achieved through the term \mathbf{F}_e^* , which is treated through the solution of a Riemann problem as described at the end of this Appendix. Through \mathbf{F}_e^* at $x = x_1^l$ (inlet) and $x = x_{N_{el}}^u$ (outlet) we are also able to enforce inflow and outflow boundary conditions and connect Ω to other domains in the arterial network, as described in Section 2.6.

The term \mathbf{F}_v^* requires a different treatment. Various ways of dealing with \mathbf{F}_v^* are analysed in [185] and the references therein. Here, we approximate \mathbf{F}_v^* at the inter-element boundaries as

$$\mathbf{F}_v^*|_{x_e^u} = \mathbf{F}_v^*|_{x_{e+1}^l} = \frac{1}{2} \left(\mathbf{F}_v|_{x_e^u} + \mathbf{F}_v|_{x_{e+1}^l} \right), \quad e = 1, \dots, N_{el} - 1,$$

with $\mathbf{F}_v^*|_{x_1^l} = \mathbf{F}_v|_{x_1^l}$ at the inlet of the domain and $\mathbf{F}_v^*|_{x_{N_{el}}^u} = \mathbf{F}_v|_{x_{N_{el}}^u}$ at the outlet, so that $\mathbf{F}_v^* - \mathbf{F}_v(\mathbf{U}^{\delta}) = 0$ at both boundaries; *i.e.* visco-elasticity is neglected when enforcing the boundary

conditions and connecting arterial segments through junctions (see Section 2.6).

We select the expansion bases to be a polynomial space of order \mathcal{P} and expand the solution on each region Ω_e in terms of Legendre polynomials $L_j(\xi)$ of order \mathcal{P} ; *i.e.*

$$\mathbf{U}^\delta|_{\Omega_e}(x_e(\xi), t) = \sum_{j=1}^{\mathcal{P}} L_j(\xi) \hat{\mathbf{U}}_e^j, \quad (28)$$

where $\hat{\mathbf{U}}_e^j(t)$ are the expansion coefficients. Following standard finite element techniques, we use the elemental affine mapping $x_e(\xi) = x_e^l \frac{(1-\xi)}{2} + x_e^u \frac{(1+\xi)}{2}$, with ξ in the reference element $\Omega_{\text{st}} = \{-1 \leq \xi \leq 1\}$. Legendre polynomials are particularly convenient because they are orthogonal with respect to the $L^2(\Omega_e)$ inner product, leading to an explicit system of equations. Substitution of (28) into (27) and letting $\boldsymbol{\psi}^\delta|_{\Omega_e} = \mathbf{U}^\delta|_{\Omega_e}$, yields $2\mathcal{P}$ equations to be solved for each Ω_e , $e = 1, \dots, N_{\text{el}}$,

$$\frac{d\hat{U}_{i,e}^j}{dt} = \mathcal{G}(\mathbf{U}^\delta|_{\Omega_e})_i, \quad j = 1, \dots, \mathcal{P}, \quad i = 1, 2, \quad (29)$$

where $\hat{U}_{i,e}^j$ ($j = 1, \dots, \mathcal{P}$; $i = 1, 2$; $e = 1, \dots, N_{\text{el}}$) are the two components of $\hat{\mathbf{U}}_e^j$,

$$\mathcal{G}(\mathbf{U}^\delta|_{\Omega_e})_i = - \left(\frac{\partial F_i}{\partial x}, L_p \right)_{\Omega_e} - \left[\frac{1}{J_e} L_p [F_i^* - F_i(\mathbf{U}^\delta|_{\Omega_e})] \right]_{x_e^l}^{x_e^u} + (\hat{S}_i(\mathbf{U}_e^\delta), L_p)_{\Omega_e},$$

and $J_e = \frac{1}{2}(x_e^u - x_e^l)$ is the Jacobian of the elemental mapping from the standard element Ω_{st} . For every Ω_e , $\mathbf{U}^\delta|_{\Omega_e}$ is evaluated at Gauss-Lobatto-Legendre quadrature points of order \mathcal{Q} to calculate the integrals $(\frac{\partial F_i}{\partial x}, L_p)_{\Omega_e}$ and $(\hat{S}_i, L_p)_{\Omega_e}$. All spatial derivatives are calculated using collocation differentiation at the quadrature points [186].

To advance in time we use an explicit second-order Adams-Bashforth scheme, with zero pressures and velocities as initial conditions. If the viscous term in the tube law (4) is neglected (*i.e.* we have a purely elastic law), then the time step Δt can be about an order of magnitude greater than that used for the visco-elastic case, since the convection Δt scales like the square of the polynomial order \mathcal{P} , whereas the diffusion Δt scales like twice the square of \mathcal{P} [186]. Although Δt has to be reduced in the visco-elastic model, it is still practical to use an explicit scheme if \mathcal{P} are small (2 or 3), because wave speeds c are much larger than flow velocities U .

We calculate the initial areas $A_0(x)$ that will give the areas $A_{\text{ref}}(x)$ at a given mean pressure P_{ref} (*e.g.* 95 mmHg for the diameters of the 55-artery model shown in Table 1) using

$$A_0 = A_{\text{ref}} \left(1 - \sqrt{A_{\text{ref}} \frac{P_{\text{ref}} - P_{\text{ext}}}{\beta}} \right). \quad (30)$$

This expression follows from combining Eqs. (5) and (13) with $P_e = P_{\text{ref}}$ and $A = A_{\text{ref}}$. It provides an approximated A_0 since our tube law is nonlinear.

The Riemann problem

Consider two area and velocity states (A_L, U_L) and (A_R, U_R) separated by an interface at time t (Fig. 13). In Eq. (27) these states are located at the end point of Ω_e and initial point of Ω_{e+1} for $e = 1, \dots, N_{\text{el}} - 1$ (Fig. 13, middle). If β and A_0 are discontinuous across the interface, two new states, (A_L^*, U_L^*) and (A_R^*, U_R^*) , originate on each side of the interface at time $t + \Delta t$. To determine them we apply Eq. (11) on each side of the interface, assuming $\mathbf{S} = 0$ and zero wall viscosity,

$$W_f(A_L^*, U_L^*) = W_f(A_L, U_L), \quad W_b(A_R^*, U_R^*) = W_b(A_R, U_R), \quad (31)$$

and conservation of mass and continuity of the (dynamic plus kinematic) pressure at the interface,

$$A_L^* U_L^* = A_R^* U_R^*, \quad \rho \frac{(U_L^*)^2}{2} + P_e(A_L^*) = \rho \frac{(U_R^*)^2}{2} + P_e(A_R^*). \quad (32)$$

Solving Eqs. (31) and (32) at the interface of Ω_e and Ω_{e+1} using the iterative Newton-Raphson method (with the initial guesses (A_L, U_L) and (A_R, U_R)) allows us to calculate the approximated elastic flux on each side of the interface; *i.e.* $\mathbf{F}_e^*|_{x_e^u} = \mathbf{F}_e(A_L^*, U_L^*)$ and $\mathbf{F}_e^*|_{x_{e+1}^l} = \mathbf{F}_e(A_R^*, U_R^*)$.

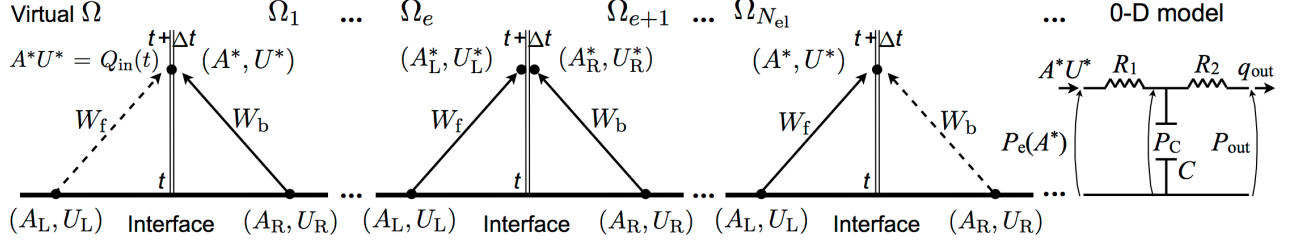


Figure 13: Layout of the Riemann problems solved at the inlet of the ascending aorta (left), elemental interfaces of each arterial segment Ω (middle), and 1-D model terminal branches (right) to calculate the states at time $t + \Delta t$: (left) (A^*, U^*) satisfying $A^*U^* = Q_{in}$, where $Q_{in}(t)$ is the prescribed volume flow (left), (middle) (A_L^*, U_L^*) and (A_R^*, U_R^*) , and (right) (A^*, U^*) , with A^*U^* and $P_e(A^*)$ related through a 0-D model. These states originate from the discontinuity between (A_L, U_L) and (A_R, U_R) at time t . Here we couple a 0-D RCR model to simulate the downstream vasculature, which consists of two resistances, R_1 and R_2 , and one compliance, C . The pressure at which flow to the microcirculation ceases is P_{out} .

The fluxes \mathbf{F}_e^* at the inlet ($x = x_1^l$) and outlet ($x = x_{N_{el}}^u$) of every arterial domain Ω are calculated through the solution of a Riemann problem involving suitable boundary conditions, as detailed in the next sections of this appendix. For these problems β and A_0 have the same value on both sides of the interface, so that $\frac{d\mathbf{W}}{dt} = \mathbf{0}$ applies across the interface, according to (11). Thus, $W_f(A_L, U_L) = W_f(A_R^*, U_R^*)$ and $W_b(A_R, U_R) = W_b(A_L^*, U_L^*)$, which combined with (31) yield a unique state (A^*, U^*) on both sides of the interface, with

$$A^* = \left[\frac{W_f(A_L, U_L) - W_b(A_R, U_R)}{8} \sqrt{\frac{2\rho A_0}{\beta}} + A_0^{1/4} \right]^4, \quad (33)$$

$$U^* = \frac{W_f(A_L, U_L) + W_b(A_R, U_R)}{2}. \quad (34)$$

For more general techniques to solve the Riemann problem, which capture shock waves originated at the interfaces, see [187, 188]. Shocks, however, rarely, if ever, occur in arteries despite the dependence of c on P , since pulse wavelengths are much larger than arterial lengths.

Inflow boundary condition (Section 2.6.1)

To prescribe $Q_{in}(t)$ at the inlet of an arterial domain Ω , we solve a Riemann problem (Fig. 13, left), with (A_R, U_R) the first point in the elemental region Ω_1 and (A_L, U_L) a virtual point outside Ω , the same β and A_0 on both sides of the interface, and $A_L = A_R$. We calculate the unique state (A^*, U^*) at time $t + \Delta t$ from $A^*U^* = Q_{in}$ and $W_b(A^*, U^*) = W_b(A_R, U_R)$, which combine to yield

$$U^* = W_b(A_R, U_R) + 4(c(A^*) - c_0), \quad (35)$$

$$Q_{in} = A^*W_b(A_R, U_R) + 4A^*(c(A^*) - c_0). \quad (36)$$

We first solve the nonlinear Eq. (36) for A^* using the iterative Newton-Raphson method with the initial guess $A^* = A_R$ and then calculate U^* using Eq. (35), so that the approximated elastic flux $\mathbf{F}_e^*|_{x_1^l} = \mathbf{F}_e(A^*, U^*)$. Note that $U_L = 2U^* - U_R$ follows from Eq. (34) with $A_L = A_R$.

Junction matching conditions (Section 2.6.2)

We can calculate the state (A^{*j}, U^{*j}) at time $t + \Delta t$ at the point of each domain Ω_j ($j = a, b, c$) adjacent to a junction from the corresponding states (A^j, U^j) at time t as follows. Applying conservation of mass and continuity of pressure (static plus dynamic) yields

$$A^{*a} U^{*a} = A^{*b} U^{*b} + A^{*c} U^{*c}, \quad (37)$$

$$P_e(A^{*a}) + \frac{1}{2} \rho (U^{*a})^2 = P_e(A^{*b}) + \frac{1}{2} \rho (U^{*b})^2, \quad P_e(A^{*a}) + \frac{1}{2} \rho (U^{*a})^2 = P_e(A^{*c}) + \frac{1}{2} \rho (U^{*c})^2, \quad (38)$$

respectively. Eq. (38) approximates the balance of energy occurring at the junction using Bernoulli's law. Assuming $\mathbf{S} = 0$ within the points adjacent to the junction, the correct propagation of characteristic information in each domain Ω_i requires

$$W_f(A^{*a}, U^{*a}) = W_f(A^a, U^a), \quad W_b(A^{*b}, U^{*b}) = W_b(A^b, U^b), \quad W_b(A^{*c}, U^{*c}) = W_b(A^c, U^c) \quad (39)$$

for the splitting flow case and

$$W_b(A^{*a}, U^{*a}) = W_b(A^a, U^a), \quad W_f(A^{*b}, U^{*b}) = W_f(A^b, U^b), \quad W_f(A^{*c}, U^{*c}) = W_f(A^c, U^c) \quad (40)$$

for the merging flow case. The resulting nonlinear system of six equations ((37), (38) and (39) or (37), (38) and (40)) and six unknowns (A^{*j}, U^{*j}) , $j = a, b, c$, at each junction in the network is solved using a Newton-Raphson method with the initial guess (A^j, U^j) , $j = a, b, c$. Thus, we can calculate \mathbf{F}_e^* at the point of each domain Ω_j ($j = a, b, c$) adjacent to the junction.

Terminal boundary conditions (Section 2.6.3)

At the outflow of 1-D model terminal branches we couple 0-D models of the perfusion of downstream vessels through the solution of a Riemann problem at the 1-D/0-D interface (Fig. 13, right). An intermediate state (A^*, U^*) originates at time $t + \Delta t$ from the states (A_L, U_L) , which corresponds to the end point of the 1-D domain, and (A_R, U_R) , which is a virtual state selected so that (A^*, U^*) satisfies the relation between A^* and U^* dictated by Eq. (14), with $Q = A^* U^*$ and $P_e = \frac{\beta}{A_0} (\sqrt{A^*} - \sqrt{A_0})$. The initial resistance, R_1 , satisfies

$$A^* U^* = \frac{P_e(A^*) - P_C}{R_1}, \quad (41)$$

where P_C is the pressure at C . The CR_2 system is governed by

$$C \frac{dP_C}{dt} = A^* U^* - \frac{P_C - P_{out}}{R_2}. \quad (42)$$

At every time step n , P_C is calculated by solving a first-order time discretisation of (42), $P_C^n = P_C^{n-1} + \frac{\Delta t}{C} \left(A_L U_L - \frac{P_C^{n-1} - P_{out}}{R_2} \right)$, with $P_C^{n-1} = 0$ for $n = 1$.

To close the problem we consider that β and A_0 are the same on both sides of the interface, $W_f(A^*, U^*) = W_f(A_L, U_L)$, and $A_R = A_L$. This yields a nonlinear equation in A^* ,

$$\mathcal{F}(A^*) = R_1 [U_L + 4c(A_L)] A^* - 4R_1 c(A^*) A^* - \frac{\beta}{A_0} (\sqrt{A^*} - \sqrt{A_0}) + P_C^n = 0, \quad (43)$$

which is solved using Newton's method with the initial guess $A^* = A_L$. Once A^* has been obtained, U^* is calculated as $U^* = \frac{P_e(A^*) - P_{out}}{A^* R_1}$, so that $\mathbf{F}_e^*|_{x_{N_{el}}^u} = \mathbf{F}_e(A^*, U^*)$ in the last point of the 1-D model terminal branch. A numerical analysis of this coupling is given in [189].

Appendix 3: Reflection coefficients at junctions

Consider three arterial segments Ω^j , $j = a, b, c$, joining in a splitting or merging flow junction (Fig. 5). Three perturbations $(\Delta a^j, \Delta p_e^j, \Delta q^j)$ of the initial states $(A^j, P_e^j, Q^j) = (A_0^j, 0, 0)$, $j = a, b, c$, propagating toward the junction (along each corresponding segment Ω^j) will produce a new wave in each segment, denoted by $(A_0^j + \delta a^j, \delta p_e^j, \delta q^j)$, $j = a, b, c$, which will propagate away from the junction. These new waves can be calculated using the linearised 1-D equations (15) as follows.

Neglecting second order terms, conservation of mass and continuity of the total pressure yield

$$\delta q^a = \delta q^b + \delta q^c, \quad (44)$$

$$\delta p_e^a = \delta p_e^b = \delta p_e^c \equiv \delta p_e. \quad (45)$$

For a splitting flow junction (Fig. 5, left), we require the following relation between the linear characteristic variables (17) moving towards the junction,

$$\delta q^a + \frac{\delta p_e^a}{Z_0^a} = \Delta q^a + \frac{\Delta p_e^a}{Z_0^a}, \quad \delta q^b - \frac{\delta p_e^b}{Z_0^b} = \Delta q^b - \frac{\Delta p_e^b}{Z_0^b}, \quad \delta q^c - \frac{\delta p_e^c}{Z_0^c} = \Delta q^c - \frac{\Delta p_e^c}{Z_0^c}, \quad (46)$$

where Z_0^j , $j = a, b, c$, is the characteristic impedance of each corresponding segment Ω^j . Moreover,

$$\Delta q^a = \frac{\Delta p_e^a}{Z_0^a}, \quad \Delta q^b = -\frac{\Delta p_e^b}{Z_0^b}, \quad \Delta q^c = -\frac{\Delta p_e^c}{Z_0^c}, \quad (47)$$

since the initial characteristic variables moving away from the junction are all zero; *i.e.* $w_b^a = 0$, $w_f^b = 0$ and $w_f^c = 0$ (see Eq. (17)). Combination of Eqs. (46) and (47) yields

$$\delta q^a = 2\frac{\Delta p_e^a}{Z_0^a} - \frac{\delta p_e^a}{Z_0^a}, \quad \delta q^b = -2\frac{\Delta p_e^b}{Z_0^b} + \frac{\delta p_e^b}{Z_0^b}, \quad \delta q^c = -2\frac{\Delta p_e^c}{Z_0^c} + \frac{\delta p_e^c}{Z_0^c}. \quad (48)$$

Substitution of these expressions into Eq. (44) and using Eq. (45) leads to

$$\delta p_e = \delta p_e^a = \delta p_e^b = \delta p_e^c = \frac{2(Y_0^a \Delta p_e^a + Y_0^b \Delta p_e^b + Y_0^c \Delta p_e^c)}{Y_0^a + Y_0^b + Y_0^c}, \quad (49)$$

where $Y_0^j = 1/Z_0^j$, $j = a, b, c$, is the characteristic admittance of each corresponding segment Ω^j .

If we perturb one segment at a time with $(\Delta a^j, \Delta p_e^j, \Delta q^j)$, $j = a, b, c$, so that $\Delta p_e^i = 0$ for $i \neq j$, then from Eq. (49) we have

$$\delta p_e^j = \frac{2Y_0^j \Delta p_e^j}{Y_0^a + Y_0^b + Y_0^c}, \quad j = a, b, c. \quad (50)$$

Defining the reflection coefficients R_f^j , $j = a, b, c$, as the ratio of the change of pressure across the reflected wave to the change of pressure in the incident wave; *i.e.* $R_f^j \equiv (\delta p_e^j - \Delta p_e^j) / \Delta p_e^j$, $j = a, b, c$, we obtain Eq. (19) from Eq. (50).

For a merging flow junction (Fig. 5, right), Eqs. (44) and (45) are still valid, whereas Eqs. (46) and (47) respectively become

$$\delta q^a - \frac{\delta p_e^a}{Z_0^a} = \Delta q^a - \frac{\Delta p_e^a}{Z_0^a}, \quad \delta q^b + \frac{\delta p_e^b}{Z_0^b} = \Delta q^b + \frac{\Delta p_e^b}{Z_0^b}, \quad \delta q^c + \frac{\delta p_e^c}{Z_0^c} = \Delta q^c + \frac{\Delta p_e^c}{Z_0^c}, \quad (51)$$

$$\Delta q^a = -\frac{\Delta p_e^a}{Z_0^a}, \quad \Delta q^b = \frac{\Delta p_e^b}{Z_0^b}, \quad \Delta q^c = \frac{\Delta p_e^c}{Z_0^c}. \quad (52)$$

Combining Eqs. (44), (45), (51) and (52) as described above for the splitting flow case also yields

Eq. (19).

Note that from $p_e = \frac{a}{C_{1D}}$ in Eq. (15) we have $\Delta p_e^j = \Delta a^j / C_{1D}^j$ and $\delta p_e^j = \delta a^j / C_{1D}^j$, $j = a, b, c$. Thus, $R_f^j = (\delta a^j - \Delta a^j) / \Delta a^j$, $j = a, b, c$, is satisfied, which shows that the reflection coefficients also give the ratio of the change of area across the reflected wave to the change of area in the incident wave. However, in terms of changes in the flow rates we have $R_f^j = -(\delta q^j - \Delta q^j) / \Delta q^j$, $j = a, b, c$, which follows from transforming δq^j and Δq^j into pressures using Eqs. (47) and (48) for the splitting flow case and Eqs. (51) and (52) for the merging flow case.

The transmission coefficient, T^j , of a segment Ω^j , $j = a, b, c$, defined as the ratio of the pressure perturbation transmitted to segments Ω^i ($i \neq j$) to the pressure perturbation in vessel Ω^j , is $T^j = \delta p_e^j / \Delta p_e^j = \delta p_e^j / \Delta p_e^j = 1 + R_f^j$, $j = a, b, c$.